



Cite this: *Mater. Adv.*, 2021, 2, 5274



Received 24th April 2021,  
Accepted 28th June 2021

DOI: 10.1039/d1ma00377a

rsc.li/materials-advances

## Organolead halide perovskites beyond solar cells: self-powered devices and the associated progress and challenges

Avi Mathur, † Hua Fan and Vivek Maheshwari \*

Conventional electronic devices powered by lithium-ion batteries or supercapacitors face the challenge of offering long-term and self-sustaining operations. Self-powered devices based on emerging energy harvesting technologies can help of the development of long-lasting transducers with a small form factor. Organolead halide perovskites due to their excellent electro-optical properties are promising photosensitive materials for the development of such self-powered devices. The following review aims at summarizing recent developments made in the field of organolead halide perovskite based self-powered applications. The underlying mechanism driving the self-powered operation in electronic devices such as photodetectors, tactile sensors, and gas sensors is discussed in detail. Finally, the current challenges and prospects of these perovskite based optoelectronic applications are highlighted.

## Introduction

With the ongoing continuous advancement in the fields of the Internet of Things (IoT),<sup>1–3</sup> portable and wearable electronic devices,<sup>4,5</sup> structural monitoring,<sup>6,7</sup> and implantable medical

Department of Chemistry, Waterloo Institute for Nanotechnology,  
University of Waterloo, 200 University Ave. West, Waterloo, ON, N2L 3G1, Canada.  
E-mail: vmahehw@uwaterloo.ca

† A. M. and H. F. contributed equally to this work.



Avi Mathur

Indian Institute of Science, Bangalore, India. He has authored 6 original research articles so far. His research interests include organic–inorganic hybrid perovskites for photovoltaic and optoelectronic device applications.

Avi Mathur was born in Khairthal, India. He received his BTech degree in information and communication technology and MTech degree in nanotechnology from the University of Rajasthan, Jaipur. He is currently pursuing a PhD degree in chemistry (nanotechnology) from the University of Waterloo, Canada. Before joining the doctoral program, Avi served as a Project Research Assistant at the Nanoscale Devices Laboratory,

devices,<sup>8,9</sup> the indispensable dependence of electronic devices and sensors on an external source of power poses a significant challenge. As it stands, electronic devices and sensors, especially those located in remote places, are powered solely by batteries. The limited lifetime of batteries mandates frequent replacement, and, more importantly, batteries also pose a risk of leaking toxic hazardous substances into the environment.<sup>10,11</sup> Therefore, concurrently with the current efforts for the miniaturization of sensors and integrated circuits,<sup>12</sup> there is an equally critical need for transducers that are capable of operating by harvesting power



Hua Fan

Hua Fan received her MS in applied chemistry from Beihang University in 2016. She is currently a PhD candidate in chemistry at the University of Waterloo. Her research interests include 1D nanomaterials, flexible devices, and wearable electronics.

solely from the ambient environment. Such an approach not only will help in reducing the load drawn from batteries or supercapacitors but can very well eliminate the need for an external power supply as well.

Self-powered devices, as the name indicates, do not need an external power source for their operation. They instead harvest energy needed for their operation from the ambient environment using stimuli such as light, heat, mechanical modulations (*e.g.* vibrations, stress), and humidity variations.<sup>13</sup> With the advancement in the field of designing integrated circuits with low power requirements, an increasing number of electronic devices for a variety of applications are becoming feasible candidates to be self-powered.<sup>14–17</sup> Owing to its ability to power devices and sensors even in outdoor and remote locations and its widespread availability, light/solar energy harvesting provides a viable method for energy harvesting.<sup>18</sup> Furthermore, presided by the United Nations sustainability development goals, as we look forward towards achieving modern, reliable, and cost-effective energy for all, solar energy harvesting is being considered as one of the most promising technologies for long-term renewable energy production.<sup>19</sup> In this pursuit, lead halide perovskites are acknowledged as viable materials for the development of cost-effective and highly efficient photovoltaic systems. The last decade has witnessed an intense research in perovskites solar cells (predominantly with lead-halide based materials), as their certified power conversion efficiency (PCE) has exceeded 25%, up-scaled from just 3.8% within a decade, rivaling that of silicon-based solar cells.<sup>20,21</sup> In general, perovskites refer to the class of compounds with a general formula of  $ABX_3$  where A and B represent cations of dissimilar sizes while X indicates anion halides, sulfides, and oxides.<sup>22</sup> Owing to their photosensitive nature, the focus of attention has been predominantly on the organic–inorganic halide perovskites where  $A^+$  represents either a methylammonium ( $MA^+$ ) or formamidinium cation ( $FA^+$ ). The small size of the methylammonium cation ( $CH_3NH_3^+$ ) leads to the formation of a stable tetragonal phase at room temperature.<sup>23</sup> The 3-D framework of  $MABX_3$  is devoid of distortion in the MA–X interaction, as otherwise observed in systems involving ethyl ammonium ( $CH_3CH_2NH_3^+$ ) and formamidinium cation

( $HC(NH_2)_2^+$ ).<sup>24</sup> In the context of occupying the B site in the  $ABX_3$  system, lead (Pb) has been reported as the superior constituent in comparison to its IV A metal counterparts such as tin (Sn), both in terms of stability and performance and consequentially has been the most widely used metal ion. Ideally, utilization of those with lower atomic numbers (such as Ge or Sn) can be used to lower the energy bandgap of the corresponding perovskite and in addressing the toxicity of Pb, but their utilization is limited by the low intrinsic ionic stability of their divalent oxidation state.<sup>25</sup> The halide anion X provides much more freedom of variation in its composition. Iodide (I), lying closest to Pb in the periodic table, shares a similar covalent character and leads to a stable perovskite structure. Upon progressing down the VII A group elements ( $Cl \rightarrow I$ ), with an increase in the atomic size of the anion, the absorption spectra shift towards a longer wavelength (redshift) which is attributed to a decrease in electronegativity.<sup>24</sup> Hence, chloride and bromide incorporation along with the iodide anion at the X site offers a facile way to tune the bandgap of the halide perovskites. Owing to the exhibition of remarkable properties such as broad absorption spectrum, high absorption coefficient, long carrier lifetime, low trap density, and large diffusion length, organolead halide perovskites (OLHPs) are ideally suited as a material of choice for photovoltaic devices and light energy harvesting.<sup>26</sup> For instance, the  $MAPbI_3$  tetragonal phase exhibits a suitable bandgap in the range of 1.51–1.55 eV, with an 820 nm absorption edge, exceeding the optimal 1.1–1.4 eV bandgap range governed by the Shockley–Queisser limit for a single-junction solar cell.<sup>27</sup> Hence,  $MAPbI_3$  is the most typically employed OLHP in photovoltaic applications.

While significant research efforts have been devoted to enhancing the PCE of perovskite solar cells (PSC), new applications of these materials are being researched with increasing efforts, for instance, lasers, light-emitting diodes (LEDs), photodetectors (PDs), gas sensors and tactile sensors.<sup>28–33</sup> In the past few years, OLHP based optoelectronic devices and sensors, capable of operating without an external power supply and exhibiting excellent performance, have been actively researched and reported, continuously advancing the field of self-powered devices.<sup>34</sup> Therefore, a review focusing on OLHP based self-powered devices will be useful for researchers in this field and also the broader research community. This review provides a detailed discussion of the mechanisms driving self-powered operation in OLHP based electronic devices of varying architecture and their associated figures of merit. Understanding these ongoing developments of perovskite-based self-driven devices will pave the way for further optimization and advancements in this area for future commercialization. A wide array of applications beyond solar cells are discussed where OLHP harvests energy and simultaneously serves as an active layer in an integrated device. A limited discussion focuses on cases where OLHP harvests energy and drives an independent device. Primarily, the latest advancements in PDs, IoTs, transistors, photovoltaic cells, and sensors are reviewed. Finally, the current challenges of the perovskite-based self-



Vivek Maheshwari

Vivek Maheshwari is an associate professor of chemistry at the University of Waterloo. He is also a member of the Waterloo Institute for Nanotechnology. His group's research is on lead halide perovskite materials for devices and sensors, 1D materials for wearable devices, and nanomaterials for electrocatalysis. He completed his bachelor's degree from the Indian Institute of Technology, Delhi, and his doctorate from Virginia Tech.

powered devices are presented along with a discussion on future research prospects.

## 1. Photodetector (PD)

A PD converts an optical input such as visible light photons into an electrical signal<sup>35</sup> and has wide-ranging applications in the detection of light intensity, spectral range detection,<sup>36</sup> thermal imaging,<sup>37</sup> remote imaging,<sup>38</sup> and so forth. The significant figures of merit for PDs include responsivity, detectivity, light switching ratio (on/off ratio), spectral selectivity, linear dynamic range, and response time.<sup>39</sup> Currently, most of the commercial photodetectors are based on crystalline GaN, Si, and InGaAs.<sup>40</sup> The underlying mechanism driving the PD operation is either a p-n (p-i-n) junction, Schottky based, or a photoconductive effect, where the conductivity of the active material increases on interaction with the incident photons. Broad spectral range (190–1100 nm) commercial photodetectors based on the Si p-n junction (photodiodes) (e.g., Hamamatsu S1336) exhibit peak responsivities of 0.12 and 0.5 A W<sup>-1</sup> at 200 and 960 nm, respectively, and those designed especially for the visible range (340–720 nm) photometry (e.g., Hamamatsu S8265) exhibit a responsivity of 0.3 A W<sup>-1</sup> at the peak sensitivity wavelength of 540 nm, with a dark current of ~20 pA. These commercial PDs usually require an external power supply and hence need an integrated assembly in the device which can make the device bulky and serve as a bottleneck for utilization in a remote location. Furthermore, these commercial photodiodes need stringent manufacturing controls which limit them to low-volume, high-value markets. To overcome the existing trade-offs between performance, form factor, cost, and most importantly, power consumption, self-powered PDs are being investigated with intense interest.<sup>41–43</sup> Self-driven PDs can be obtained when photodiodes work at zero bias, similar to solar cells working under short-circuit conditions. Owing to their excellent electro-optical characteristics, the OLHP based self-powered PDs can offer the benefit of being lightweight with a small device size, without compromising on device performance.<sup>44</sup> The early reports on perovskite-based PDs with self-powered characteristics (but did not focus on it exclusively) appeared in 2014 when Dou *et al.* demonstrated a solution processed 'inverted' device (solar cell) configuration PD based on organic-inorganic hybrid  $\text{CH}_3\text{NH}_3\text{PbI}_{3-x}\text{Cl}_x$ . The device had a high detectivity of up to  $10^{14}$  Jones and was capable of operating at 0 V.<sup>45</sup> Based on the charge separation mechanism, OLHP PDs can generally be classified into the following categories: p-n (or p-i-n) junction, Schottky junction, polarization effects based, and photoelectrochemical-type PDs. Besides these, an integrated system of energy harvesting units (such as TENG) that drives the light sensitive OLHP to achieve detection can be considered as a distinct type of self-driven PD. The following section summarizes recent advances in PDs driven by these operating mechanisms. Some common strategies that are being employed for enhancing the figures of merit for perovskite PDs have also been discussed. The last subsection is

dedicated to flexible OLHP PDs that are now receiving substantial attention as promising candidates for next-generation portable and wearable electronics.

### 1.1 p-n (or p-i-n) junction-based PDs

The p-n junction-based PDs are the most common type reported so far in the literature. A typical PD with a vertical architecture consists of a perovskite layer sandwiched between an electron transport layer (ETL) and a hole transport layer (HTL) (p-i-n type). It is widely accepted that the interfacial contact properties between the perovskite and transport layers affect the efficiency of photovoltaic devices. Hence, by careful selection of the transport layers, PDs with effective dissociation and transport of photogenerated charge carriers to their respective counter electrode contacts can be fabricated.<sup>46</sup> ETLs not only influence the electron transfer and collection but also behave as the hole blocking layer to suppress the electron–hole recombination at the interface.<sup>47,48</sup> Significant attention has been paid to ZnO as an electron transport material (ETL) in the early research works reporting OLHP based self-powered PDs. Specifically, morphological tuning of ZnO material was used for the performance optimization of OLHP PDs. Initially, Wang *et al.* coupled the pyroelectric effect generated in wurtzite ZnO nanowires (NWs) with the photoexcitation ability of MAPbI<sub>3</sub>.<sup>49</sup> The assembly with well-aligned energy band levels led to enhanced charge-carrier separation at the ZnO/perovskite interface. The perovskite also contributed to low dark currents and low background temperature. In the self-powered mode, this UV sensitive heterostructure assembly exhibited 322% enhancement in specific detectivity and responsivity, complemented with five orders of magnitude improvement in the rise time (5.4 s to 53  $\mu$ s) and fall time (8.9 s to 63  $\mu$ s) in comparison to devices operating at an applied bias of 0.3 V. The decline in device performance due to applied bias was attributed to the reduced pyro-potential of ZnO NWs owing to the high dark currents and high background temperature. Another report on well-aligned energy levels in the ZnO nanorod (NR)/MAPbI<sub>3</sub> heterostructure appeared a year later. Here, Yu *et al.* used an inorganic metal oxide layer of MoO<sub>3</sub> as a hole transport layer to enhance exciton transport while simultaneously protecting the organic perovskite layer.<sup>50</sup> The corresponding broadband PD with an appropriate thickness of MoO<sub>3</sub> (12 nm) yielded a high detectivity value of  $3.56 \times 10^{14}$  Jones and 24.3 A W<sup>-1</sup> photo-responsivity under 500 nm excitation and no applied bias. Other than preferable band alignment, Zhu *et al.* proposed the hypothesis that a uniformly distributed blend of ZnO microspheres and nanosheets can effectively utilize the high surface area of microspheres while decreasing series resistance in a vertically configured glass/fluorine doped tin oxide (FTO)/ZnO/MAPbI<sub>3</sub>/MoO<sub>3</sub>/Au device.<sup>51</sup> Under illumination, the self-driven PD exhibited spectral response from 300 to 800 nm with responsivity and detectivity values reported as high as 48 mA W<sup>-1</sup> and  $4.5 \times 10^{11}$  Jones, respectively. The on/off ratio was up to 1400, while the rise time and fall time of the photoresponse were recorded to be 14 and 12 ms, respectively. Despite the facile synthesis process and high electron mobility with increased area of



contact of the ZnO NR layer, the photoelectric performance of PDs is generally limited. This is due to the presence of defect states, especially oxygen vacancy which may lead to enhanced charge recombination at the interface between perovskite and ZnO NRs. To primarily reduce the defect density, Zhou *et al.* doped ZnO with a slightly smaller Ga<sup>3+</sup>.<sup>52</sup> The Ga doped ZnO NR layer (as ETL) served as an effective scaffold with enhanced electron mobility. The resultant HTL-free PD device prepared using graphite electrode had an on/off ratio, a responsivity, and a detectivity of  $\sim 2.5 \times 10^3$ , 0.3 A W<sup>-1</sup>, and  $1.3 \times 10^{12}$  Jones, respectively. The work by Yang *et al.* involved the coupling of a MgO/ZnO bilayer with the perovskite layer.<sup>53</sup> The ZnO microsphere array scaffold facilitated the penetration of the perovskite into the array and resulted in improved light-harvesting, while MgO passivated the interface between ZnO and perovskite, enhancing stability and carrier transport. Recently, Liu *et al.* proposed a Cu ion-induced p-type doping in perovskite films by the addition of CuSCN.<sup>54</sup> The CH<sub>3</sub>NH<sub>3</sub><sup>+</sup> cations from the perovskite film reacted with the SCN<sup>-</sup> anions from the CuSCN dopant to form HSCN and CH<sub>3</sub>NH<sub>2</sub> by-products, leaving Cu ions to get incorporated into the final perovskite film. The p-type doping facilitated hole transport at the p-n heterojunction interface of perovskite/[6,6]-phenylC<sub>60</sub>-butyric acid methyl ester (PCBM, ETL) in a self-powered HTL free PD. The authors utilized the optimized PD as a light signal receiver for transmitting text and audio signals in a homemade visible light communication system. Zhou *et al.* coupled C<sub>60</sub> as an ETL along with the perovskite/GaN heterostructure.<sup>55</sup> A direct bandgap of 3.4 eV with impressive electro-optical properties, a high carrier mobility, a high melting point, and the chemically stable nature (weak oxidation of N) motivated the authors to choose p-type GaN as the HTL in the hybrid perovskite PD. The high electron mobility and conductivity of C<sub>60</sub> enhanced the collection of the electrons along with reduced non-radiative recombination enabling self-powered characteristics. The best performing PD exhibited a responsivity of 0.198 A W<sup>-1</sup> and a detectivity of  $7.96 \times 10^{12}$  Jones with an on/off ratio  $> 5000$ . To achieve excellent PD device performance, selection of HTL is equally crucial, not only to extract the holes and decrease the dark current density but also to enhance and promote perfect light absorption by the perovskite layer in the whole visible region. Ghosh *et al.* fabricated an ETL-free self-biased PD inverted device by functionalizing HTL with plasmonic Ag nanoparticles (NPs).<sup>56</sup> The plasmon-enhanced optical absorption combined with improvement in charge extraction and transport by Ag NPs was attributed for the enhanced self-powered responsivity in the resultant PD (0.25 A W<sup>-1</sup>) with a detectivity as high as  $1.53 \times 10^{11}$  Jones. Shin *et al.* integrated graphene quantum dots (QDs) in both the HTL and photoactive MAPbI<sub>3</sub> layer.<sup>57</sup> The improved crystallinity of perovskite grains upon the integration of graphene QDs was accredited to the presence of hydrophilic groups including -OH, -COOH, and C=O that leads to the formation of strong bonds within the perovskite film. It was proposed that the addition of graphene QDs increased the work function of the HTL leading to reduced charge recombination at the perovskite/HTL interface. The corresponding self-powered rigid and flexible PDs exhibited detectivities

of  $8.7 \times 10^{12}$  and  $8.42 \times 10^{12}$  Jones, respectively, with an identical response time of 0.96  $\mu$ s at 0 V. The flexible PDs displayed appreciable bending stability by maintaining  $\sim 80\%$  of their original responsivity values after repeated bending for 1000 cycles at a radius of 4 mm. Cheng *et al.* carried out hydrothermal etching of monocrystalline silicon to prepare an array of silicon nanoporous pillars (Si-NPA) which was later used as a substrate as well as a HTL in an inverted assembly of Si-NPA/MAPbI<sub>3</sub>/ZnO PD.<sup>58</sup> The air-stable inorganic HTL enabled the PD to retain 92% performance despite storing the device in ambient air for a month. The template of quasi-identical micron-sized Si pillars offered a large interfacial contact area for incident light while simultaneously reducing the reflection. The authors proposed that the Si-NPA template also effectively enhanced carrier transport and reduced the collection path of the photogenerated carriers leading the self-driven PDs to exhibit a high on/off ratio of  $8.2 \times 10^4$ , a photoresponsivity of 8.13 mA W<sup>-1</sup>, a specific detectivity of  $9.74 \times 10^{12}$  Jones, and fast response speeds of 253.3/230.4  $\mu$ s at zero bias under 780 nm light illumination.

Towards realizing the commercial applications of self-driven PD based on OLHP, the work of Shen *et al.* can be considered as one of the most significant contributions. The authors demonstrated a homemade time-resolved photoluminescence (TRPL) system (Fig. 1a) facilitated by an ultrafast OLHP PD with the configuration of indium tin oxide (ITO)/poly(bis(4-phenyl)(2,4,6-trimethylphenyl)amine) (PTAA)/MAPbI<sub>3</sub>/C<sub>60</sub>/2,9-dimethyl-4,7-diphenyl-1,10-phenanthroline (BCP)/copper (Cu).<sup>59</sup> The device area dependent sub-nanosecond response time (0.95 ns for 0.04 mm<sup>2</sup> device area) of the PD enabled the detection of the photoluminescence lifetime for typical organic and hybrid materials, ranging from several nanoseconds to microseconds (Fig. 1b-d). In a recent work, Shan *et al.* presented a bifunctional light-emitting/detecting LiFi (light fidelity) fiber utilizing perovskite QDs.<sup>60</sup> The authors capitalized on the small exciton binding energy and high carrier mobility of the all-inorganic perovskite QDs (CsPbBr<sub>3</sub>) to successfully integrate electroluminescence with narrow emission ( $\sim 19$  nm) and photodetection in a single fiber. The flexible assembly exhibited green colored luminance of  $\sim 100$  cd m<sup>-2</sup> at 7 V after being subjected to multiple bending cycles and the corresponding current efficiency was 1.67 cd A<sup>-1</sup>. The band bending in the space charge region at the interface between the perovskite QDs and the transport layers (due to differences in the Fermi levels) enabled a zero-bias operation of the PD with an on/off ratio of 1.5. OLHP QDs can potentially be utilized based on a similar principle for bifunctional devices. A major challenge that hinders the commercial viability of OLHP PDs (and other devices) is their instability in air and under ambient conditions. OLHP material rapidly degrades and decomposes in the presence of oxygen and moisture. Furthermore, electric field induced ion migration primarily across the perovskite grain boundaries further enhances material degradation, eventually worsening the optoelectronic properties.<sup>61</sup> However, at the same time, the C-AFM and PC-AFM studies carried out by Li *et al.* in MAPbI<sub>3</sub>/CdS heterojunction PD indicated that a short transport distance at the grain boundaries acted as preferential spots of charge carrier



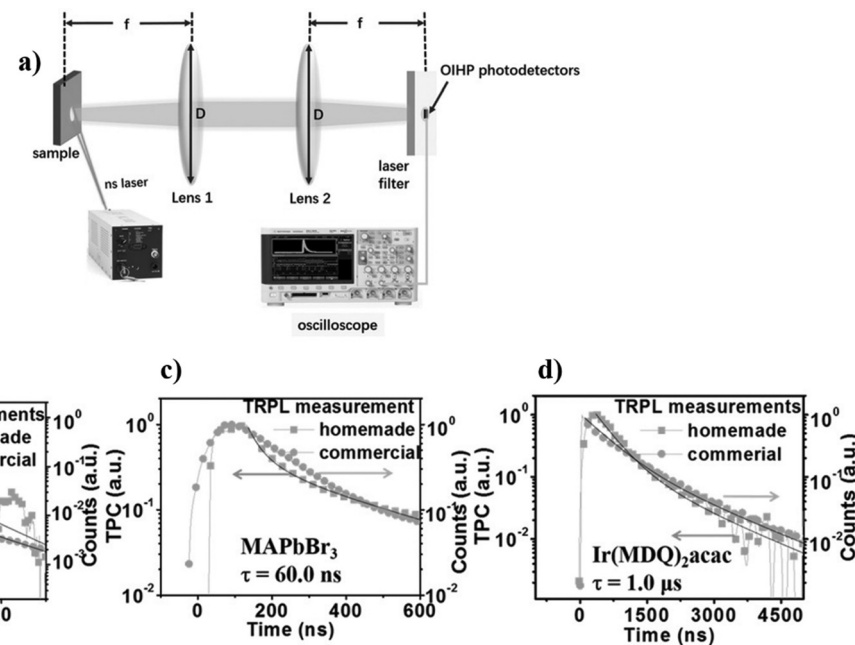


Fig. 1 Homemade time-resolved photoluminescence lifetime (TRPL) detection system with OLHP PD: (a) layout of the TRPL system. The  $\text{N}_2$  ns laser acted as an excitation source for illuminating the sample from a small angle located at the focus position of Lens 1. The OLHP photodetector receives photoluminescence from the sample once redirected by Lens 2. A filter was incorporated to filter the laser scattering emission. A 1 GHz oscilloscope with a  $50\ \Omega$  input resistance was connected to the PD to record the transient photocurrent curves. PL decay curves measured by homemade and commercial TRPL systems for (b) green polyfluorene (4.0 ns), (c)  $\text{MAPbBr}_3$  single crystal (60.0 ns) and (d) bis(2-methyldibenzo[f,h]quinoxaline) (acetylacetone) iridium(III) (1.0  $\mu$ s). The solid line is representative of exponential fitting to the data. Reproduced with permission from Shen *et al.*, *Adv. Mater.*, **28**, 10794–10800.<sup>59</sup> © 2016 Wiley-VCH Verlag GmbH & Co. KGaA, Weinheim.

transportation and exciton separation.<sup>62</sup> The study of the photoelectric mechanism at the nanoscale showed that higher photocurrent values are observed at the grain edges. This offers the potential of grain boundary engineering towards fine-tuning the overall device performance. The fabricated PD exhibited a high current on/off ratio of  $\sim 1.13 \times 10^5$ , detectivity of  $\sim 9.79 \times 10^{10}$  Jones, and PCE of up to  $\sim 10.05\%$ . Table 1 summarizes the heterojunction based self-powered OLHP PDs and their associated key figures of merit.

Although the p-n junctions have been widely applied in the fabrication of OLHP based self-driven PDs, little attention has been paid to the formation of the p-n homojunction within OLHP. Pang *et al.* stressed that the transport layers are optional

in perovskite-based optoelectronic devices and claimed that the intrinsic light-induced self-poling ability in the perovskite could drive a  $\text{Pt}/\text{CH}_3\text{NH}_3\text{PbI}_3/\text{SiO}_2/\text{Si}/\text{Al}$  configured PD.<sup>63</sup> The researchers through series of experiments ruled out the possibility of the observed self-powered characteristics being driven by the Schottky junction or poling of the device (by applying an external bias for a short duration before recording the device characteristics at 0 V). The authors hypothesized that under illumination, a built-in electric field was generated as positive ions/vacancies accumulated at the perovskite/SiO<sub>2</sub> interface and negative ions/vacancies accumulated at the perovskite/Pt interface, owing to band bending in the asymmetric device. Under the influence of the

Table 1 Summary of the p-i-n/n-i-p heterojunction based OLHP self-driven PDs and their device characteristics

Device architecture	Operating wavelength	Responsivity	Detectivity (Jones)	Light switching ratio	Response speed (rise/fall time)	Ref.
FTO/ZnO/MAPbI <sub>3</sub> /Spiro-OMeTAD/Cu	325 nm	$26.7\ \text{mA W}^{-1}$	$4.0 \times 10^{10}$		$53/63\ \mu\text{s}$	49
FTO/ZnO NR/MAPbI <sub>3</sub> /MoO <sub>3</sub> /Au	500 nm	$24.3\ \text{A W}^{-1}$	$3.56 \times 10^{14}$		$0.7/0.6\ \text{s}$	50
FTO/ZnO/MAPbI <sub>3</sub> /MoO <sub>3</sub> /Au	380 nm	$48\ \text{mA W}^{-1}$	$4.5 \times 10^{11}$		$14/12\ \text{ms}$	51
FTO/Ga <sup>3+</sup> doped ZnO NR/MAPbI <sub>3</sub> /MoO <sub>3</sub> /Au	490 nm	$0.3\ \text{A W}^{-1}$	$1.3 \times 10^{12}$	$\sim 2.5 \times 10^3$	$<2/<2\ \text{ms}$	52
FTO/ZnO/MgO/MAPbI <sub>3</sub> /C	473 nm	$5.9 \times 10^{-2}\ \text{A W}^{-1}$	$1.5 \times 10^{12}$	$7.0 \times 10^4$	$0.63/1.6\ \text{ms}$	53
ITO/MAPbI <sub>3</sub> /CuSCN/PCBM/BCP/Ag	685 nm	$0.37\ \text{A W}^{-1}$	$1.06 \times 10^{12}$		$5.02/5.50\ \mu\text{s}$	54
FTO/C <sub>60</sub> /MAPbI <sub>3</sub> /GaN	500 nm	$0.198\ \text{A W}^{-1}$	$7.96 \times 10^{12}$	$>5000$	$0.45/0.63\ \text{s}$	55
FTO/PEDOT:PSS + Ag NPs/CH <sub>3</sub> NH <sub>3</sub> PbI <sub>3</sub> /Al	400 nm	$0.25\ \text{A W}^{-1}$	$1.53 \times 10^{11}$		$110/72\ \text{ms}$	56
Al/BCP/PCBM/MAPbI <sub>3</sub> :GQDs/PEDOT: GQDs/TFSA-GR	430 nm	$0.435\ \text{A W}^{-1}$	$8.7 \times 10^{12}$		$0.56/0.96\ \mu\text{s}$	57
Planar Si/Si-NPA/MAPbI <sub>3</sub> /ZnO	780 nm	$8.13\ \text{mA W}^{-1}$	$0.974 \times 10^{13}$	$0.82 \times 10^5$	$253.3/230.4\ \mu\text{s}$	58
ITO/PTAA/MAPbI <sub>3</sub> /C <sub>60</sub> /BCP/Cu	680/700 nm	$0.47\ \text{A W}^{-1}$ ( $-0.1\ \text{V}$ )	$7.8 \times 10^{12}$ ( $-0.1\ \text{V}$ )		$0.95\ \text{ns}$	59
ITO/CdS/MAPbI <sub>3</sub> /Au	730 nm	$0.43\ \text{A W}^{-1}$	$2.3 \times 10^{11}$	$1.13 \times 10^5$	$3.2/9.6\ \text{ms}$	62



built-in electric field, the photogenerated charge carriers drifted to their respective counter electrodes. While the holes were collected by the Pt electrode, the electrons traversed through the  $\text{SiO}_2$  film and were collected by the Al electrode by the ion trap-assisted emission mechanism (Frenkel–Poole emission). By contrast, under the dark conditions,  $\text{SiO}_2$  effectively acted as an insulating layer and functioned as a barrier layer for carriers, leading to ultralow dark currents. The detectivity of the fabricated self-powered PD was measured to be  $8.8 \times 10^{10}$  Jones with a high on/off ratio of  $10^5$  at 0 V. In a separate work, Ren *et al.* deliberately transformed the top surface of the p-type perovskite ( $\text{MA}^+$  rich and  $\text{Pb}^{2+}$  deficient stoichiometry) to n-type *via* bombarding with  $\text{Ar}^+$  ions leading to the formation of a p–n homojunction within the perovskite layer.<sup>64</sup> The resultant built-in field in the perovskite promoted the separation and transport of photo-induced carriers without any external bias. The  $\text{Ar}^+$  ion bombarding facilitated  $\text{MAPbI}_3$  p–n homojunction PD exhibited an increase by one order of magnitude in the on/off ratio at 532 nm in comparison to the pristine  $\text{MAPbI}_3$  device.

## 1.2 Schottky junction-based PDs

A typical PD assembly incorporating a photosensitive semiconducting material with two ohmic metal contacts requires an external bias to drive the separation of the photogenerated electron–hole pairs. However, if one of the Ohmic contacts is replaced by a Schottky barrier contact, the built-in electrical field at that interface can lead to the separation of the photogenerated charge carriers. Unlike PDs with Ohmic contacts, the Schottky junction PDs, therefore, offer the ability to detect light irradiation without an external power supply and with high sensitivity and response speed complemented by the low dark currents. Multiple reports demonstrating the Schottky junction facilitated self-driven PDs are found in the literature. As a seminal work, the Schottky junction photodiode of the ITO/ $\text{MAPbI}_3$ /Au vertical heterostructure assembly presented by Pandey *et al.* exhibited a photosensitivity of  $1.33 \times 10^2$  with the rise time and decay time of 91 and 101 ms, respectively.<sup>65</sup> Subsequently, several important works on high-detectivity and low-noise perovskite photodiodes were reported by different research groups. The ultrahigh mobility and conductivity of multilayer graphene and its ability to form a Schottky barrier with  $\text{TiO}_2$  were combined with the high yield photocarrier transport and strong broadband light absorption capability (260–900 nm) of  $\text{CH}_3\text{NH}_3\text{PbI}_3$ , by Li *et al.*<sup>66</sup> Both graphene and perovskite act as ambipolar materials and therefore, depending on the inherent Schottky field, electrons could be transferred vertically from perovskite to  $\text{TiO}_2$  *via* the underlying graphene while the remnant holes remaining in the graphene were transferred horizontally and collected in a separate FTO electrode. The self-driven PD (FTO/ $\text{TiO}_2$ –Graphene/ $\text{MAPbI}_3$ /PTAA) demonstrated a high responsivity ( $\sim 0.375 \text{ A W}^{-1}$ ) and specific detectivity ( $\sim 10^{11}$  Jones) and an excellent on/off ratio of  $4 \times 10^6$  in comparison to the commonly used Au–perovskite–Au configuration. The protection by the top PTAA layer enabled negligible decay in the performance of the PD despite storage

under ambient conditions for 20 days and stability over 1000 cycles of operation.

Other than graphene, 2D transition-metal dichalcogenides (TMDs) are being extensively researched for a wide array of potential applications, including optoelectronics, biosensors, and piezoelectricity.<sup>67–72</sup> As a typical TMD material,  $\text{MoS}_2$  has suitable band levels and excellent charge transport properties, thus, is well suited to construct PDs based on the Schottky effect.<sup>73</sup> Bai *et al.* were amongst the first ones to use single-layer  $\text{MoS}_2$  and  $\text{MAPbI}_3$  perovskite heterojunction in a vertically configured PD.<sup>74</sup> At a light intensity of  $0.7 \text{ mW cm}^{-2}$ , the self-powered PD exhibits a responsivity of  $60 \text{ mA W}^{-1}$  with an inverse relation to power density. Zeng *et al.* combined multi-layered  $\text{PdSe}_2$ , another TMD material, with  $\text{FA}_{1-x}\text{Cs}_x\text{PbI}_3$  perovskite to achieve a Schottky junction empowered fast self-driven PD with broad spectral sensitivity (200–1550 nm).<sup>75</sup> Fig. 2a provides the schematic illustration and Fig. 2b–l represents the optoelectronic response of the  $\text{PdSe}_2$ /perovskite Schottky junction PD device. The high carrier mobility of  $\text{PdSe}_2$  and reduced surface defects at the TMD/perovskite interface enabled the Schottky junction-based  $\text{PdSe}_2$ /perovskite PD to exhibit a large on/off ratio of  $\sim 10^4$ , a high responsivity of  $313 \text{ mA W}^{-1}$  (Fig. 2j and l), a specific detectivity of  $\sim 10^{13}$  Jones (Fig. 2l), and rapid response speeds of 3.5/4  $\mu\text{s}$ . Moreover, the device exhibited sensitivity to polarized light, with a polarization sensitivity of 6.04 (Fig. 2m). To explore the infrared image sensing ability of the fabricated PD, homemade masks in the shape of alphabets such as P, O, L, Y, and U were placed between the laser illumination and the device as seen in Fig. 2n. The authors were then able to generate a 2D contrast mapping profile by plotting the dark current and photocurrent of the PD, at each pixel. Since the pixel illuminated by an 808 nm light demonstrated a considerable photocurrent of  $\sim 0.05 \mu\text{A}$ , while the rest of the area displayed negligible dark currents, the authors were able to establish that the Cs-doped  $\text{FAPbI}_3$  PD could effectively resolve images under infrared illumination (Fig. 2o).

## 1.3 Ferroelectric and polarization effect based PDs

Ferroelectrics present a promising alternative for generating power in single-phase homogeneous materials by using polarization to trigger light detection. However, the presence of the ferroelectric polarization effect in OLHP is still debatable.<sup>76–81</sup> Saraf *et al.* discussed the interplay between the polarization effect and ion migration as a function of poling conditions in  $\text{MAPbI}_3$  based PD (Fig. 3a).<sup>82</sup> The work supported the presence of ferroelectric effect in  $\text{MAPbI}_3$  as the PD poled under air and illumination lead to a ferroelectric dominated response, while poling under  $\text{N}_2$  and dark conditions leads to ion migration effects resulting in the formation of a p–n homojunction which is signified by a reversal in signs for open-circuit voltage ( $V_{oc}$ ) and short circuit current ( $I_{sc}$ ) as observed in Fig. 3b–e. To obtain a stable response, poling was done under a small external bias applied across the Au/ $\text{MAPbI}_3$ /Au configuration in air and under illumination for a short duration of 10 minutes. The poled device could then operate without requiring an external power supply for the next 2 days. Besides, the authors adopted an



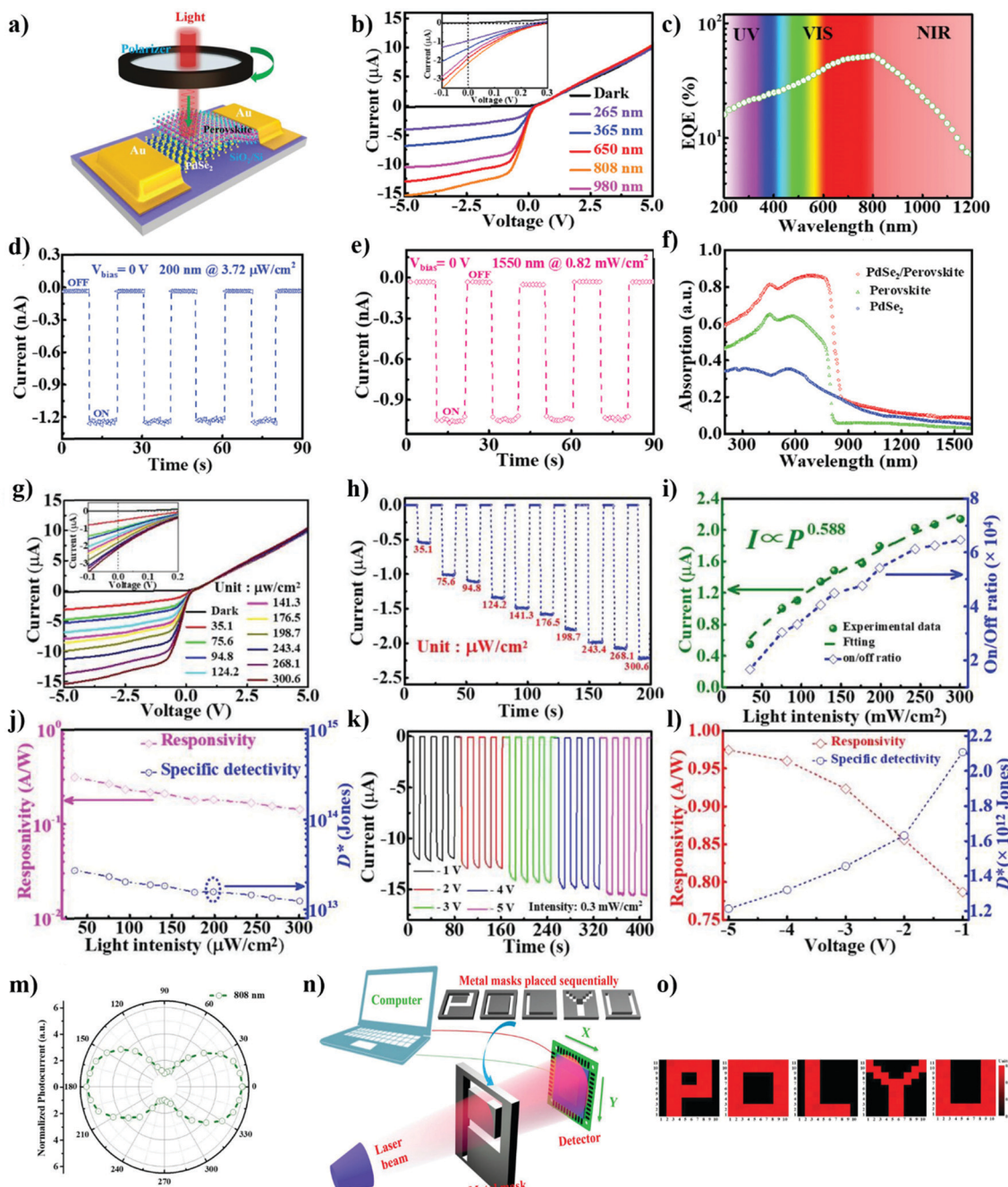


**Fig. 2** Schematic illustration and optoelectronic measurement of the PdSe<sub>2</sub>/perovskite Schottky junction PD: (a) schematic of polarized detection device based on PdSe<sub>2</sub>/perovskite. (b)  $I$ - $V$  curve in dark and under illumination with different lights. (c) Wavelength-dependent EQE at 0 V. Spectral photoresponse in the self-powered mode under (d) 200 nm ( $3.72 \mu\text{W cm}^{-2}$ ) and (e) 1550 nm ( $0.82 \text{ mW cm}^{-2}$ ) light illuminations. (f) Independent UV-Vis absorption spectrum of PdSe<sub>2</sub>, perovskite, and PdSe<sub>2</sub>/MAPbI<sub>3</sub>. (g)  $I$ - $V$  curves of PD in dark and under an 808 nm light irradiation with different intensities. (h) Time-dependent photocurrent under an 808 nm light illumination with different light intensities. (i) Photocurrent and on/off ratio as a function of light intensity at zero bias. (j) Responsivity and detectivity as a function of incident power intensity. (k) Time-dependent photocurrent at reverse bias under an 808 nm light illumination ( $0.3 \text{ mW cm}^{-2}$ ). (l) Responsivity and detectivity as a function of operating bias voltage ( $0.3 \text{ mW cm}^{-2}$ ). (m) Evolution of photocurrent as a function of different polarized angles. (n) Homemade experimental setup to realize detection ability of PdSe<sub>2</sub>/OLHP PD for NIR imaging sensing. (o) The corresponding 2D current mapping of characters "P," "O," "L," "Y," and "U" produced by an 808 nm laser. Reproduced from Zeng *et al.*, *Adv. Sci.*, **6**, 1901134.<sup>75</sup> © 2019 WILEY-VCH Verlag GmbH & Co. KGaA, Weinheim.

additive engineering strategy of integrating polystyrene (PS) in the MAPbI<sub>3</sub> films to enhance their stability. The PS-MAPbI<sub>3</sub> based planar configuration PD device illustrated an impressive

performance stability of  $>80\%$  post 20 days. On the other hand, the pristine MAPbI<sub>3</sub> counterpart device suffered from a 70–85% performance decay within 4 days of operation under similar

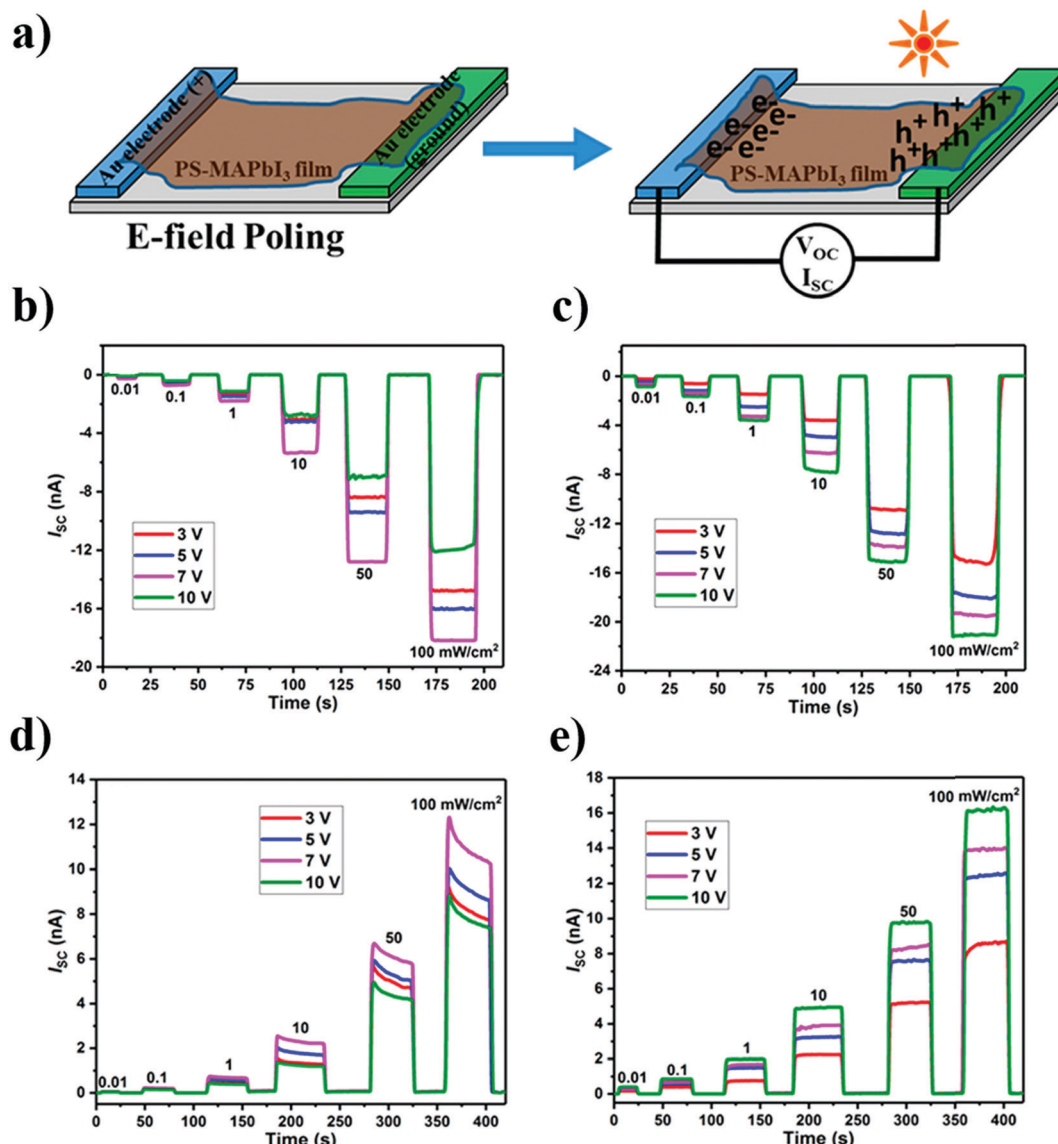


**Fig. 3** Device architecture and photoresponse after poling of MAPbI<sub>3</sub> based PD in different environments: (a) schematic diagram of the lateral self-powered PD and the effect of electric field poling leading to  $V_{oc}$  and  $I_{sc}$  response at zero bias. The  $I_{sc}$  response at 0 V from (b) MAPbI<sub>3</sub>, and (c) PS-MAPbI<sub>3</sub> devices to various light illumination intensities, post poling at different voltages for 10 min in air and under light illumination (1.0 sun). The  $I_{sc}$  response at zero bias from (d) MAPbI<sub>3</sub> and (e) PS-MAPbI<sub>3</sub>-based PDs at various light intensities after poling at different voltages under N<sub>2</sub> and dark. Reprinted with permission from R. Saraf and V. Maheshwari, *ACS Appl. Mater. Interfaces*, **10**, 21066–21072.<sup>82</sup> Copyright © 2018 American Chemical Society.

ambient conditions. The monolith PD achieved a photoresponsivity of more than  $0.61 \text{ A W}^{-1}$  and a detectivity of  $1.5 \times 10^{13} \text{ Jones}$  under such self-powered operation. Recently, utilizing the same device architecture and self-powered mechanism, Mathur *et al.*, unveiled the nanoscale tri-layer architecture of the polymer-perovskite (PS-MAPbI<sub>3</sub>) films in which the polymer forms a thin layer at the top and bottom interfaces while the perovskite forms bulk of the interlayer.<sup>83</sup> It was observed that the viscosity of the polymer chains, directly dependent on the molecular weight ( $M_w$ ) of the integrated polymer, is critical in determining the chain mobility and drives the rearrangement of the polymer chains across the perovskite film. Not only does the inclusion of varying  $M_w$  of PS (2.5, 11, 35, 61, 105, and 190 kDa) modulate the crystallization kinetics but the insulating nature of the polymer

chains also affects the charge transport. The presence of PS chains, predominantly at the grain boundaries reduces ion mobility and hence leads to reduced dark currents and ionic currents. Overall, the inclusion of intermediate  $M_w$  PS chains of 35 kDa led to optimized electro-optical properties with enhanced stability in the corresponding self-powered PD. Specifically, a 3-fold enhancement in  $I_{sc}$  (96.6 nA) and  $V_{oc}$  (162.5 mV) was observed for 35 kDa PS-MAPbI<sub>3</sub> PD in comparison to pristine MAPbI<sub>3</sub> (31.1 nA and 52.3 mV, respectively).

Irrespective of the debatable existence of ferroelectric polarization in perovskites, incorporation of an additional layer of a ferroelectric material in the perovskite PD architecture can enhance the built-in electric field leading to improved charge extraction. A report demonstrating polarization induced

internal electric field in a perovskite-based device appeared in 2018 where Cao *et al.* integrated ferroelectric  $\text{SrTiO}_3$  (STO) to serve as an interlayer in a sandwich structure of FTO/STO/MAPbI<sub>3</sub>/Spiro-OMeTAD/Ag.<sup>84</sup> The polarized STO layer provides a built-in potential and promotes downward band bending, helping to separate and transport charge carriers generated in MAPbI<sub>3</sub> upon illumination. Upon optimization of the STO layer density, the photocurrent was enhanced up to 0.956 mA with response speeds of 0.3 s (rise time) and <0.1 s (decay time) at 0 V in a PD positively poled at 1 V for 5 min. However, unlike the report of Saraf *et al.*, there was an obvious decrease in photoresponse upon exposure to air for 24 h. The substantial performance decay can be attributed to the decomposition and degradation of the OLHP active layer which is indicative of the limited stability of the fabricated PD. The authors later demonstrated a poling induced self-driven bulk heterojunction PD. This research involved the integration of another ferroelectric material P(VDF-TrFE) to enhance the strength of the ferroelectric field of the perovskite layer, facilitating better separation of the photogenerated charge carriers.<sup>85</sup> The corresponding PD exhibited high responsivity (20 mA W<sup>-1</sup>), large detectivity ( $1.4 \times 10^{13}$  Jones), and fast response speed (92/193  $\mu\text{s}$ ) at the wavelength of 650 nm. Later, the group extended the same composite assembly in the form of a nanowire array *via* an imprinting method assisted by commercially available digital versatile discs (DVD).<sup>86</sup> The resultant flexible hybrid device on the PEN substrate exhibited high detectivity ( $7.3 \times 10^{12}$  Jones), fast response time (88/154  $\mu\text{s}$ ) at zero bias, and impressive mechanical stability through bending up to 180 degrees.

#### 1.4 Triboelectric nanogenerator (TENG) based PDs

Triboelectric nanogenerators (TENGs) can act as an efficient driving source for harvesting mechanical energy to power devices such as PDs. When a physical contact occurs at the interface of two dissimilar materials, typically opposite triboelectric charges are created on the two surfaces. A mechanical motion can then induce an inherent electric potential difference capable of driving electrons back and forth between the electrodes. Su *et al.* fabricated a UV-Visible broad range PD based on the dual properties of MAPbI<sub>3</sub>: photoconductivity and surface triboelectric charge density.<sup>87</sup> An oscillating  $V_{\text{oc}}$  was generated upon the top copper electrode periodically getting into contact with the underlying perovskite layer. Upon photoexcitation, electrons from the photogenerated electron-hole pair got quickly captured by the mesoporous TiO<sub>2</sub> layer, while holes tend to partially neutralize the negative triboelectric charges present on the surface leading to an instantaneous decrease in surface charge density. The corresponding device demonstrated a responsivity of 7.5 V W<sup>-1</sup> with a response time of <80 ms. Later, Hsiao *et al.* demonstrated a similar TENG assisted perovskite PD that could generate photo response upon bending of the flexible assembly.<sup>88</sup> Guo *et al.* designed a self-powered organic optical communication system (SOCS).<sup>89</sup> This system was composed of organic light-emitting diode (OLED) driven by triboelectric nanogenerators (TENGs) and perovskite PD. In this SOCS, the mechanical signals were converted into

light by the OLED and then transferred to voltage signals by the perovskite PD. The combination of TENG with OLED exhibiting an emission peak at  $\sim 524$  nm served as a light emitter in the robotic hand, while PD served as the output voltage of SOCS with a maximum current transfer ratio of 30%. The output voltage of SOCS was modified by the different mechanical actions of the robotic hand which could be used to transmit the information on human-machine interaction.

One of the biggest limitations of conventional TENG-powered devices is their dependency on motion actuators as a power source which are prone to fluctuations due to variation in the surrounding conditions, severely hindering the accuracy of photodetection. The self-powered PD reported in work by Leung *et al.* aimed at mitigating this issue by excluding mechanical pressure being applied to the TENG (Fig. 4a-c).<sup>90</sup> The PD instead utilized the voltage regulated circuit containing a resistor and a Zener diode, which enabled uniform photodetection characteristics irrespective of irregular motion, such as human finger tapping (Fig. 4d). The fundamental principle comprised perovskite acting as a variable resistor dependent on the incident light intensity. The voltage in the photosensitive layer followed an inverse relation with light intensity owing to a decrease in resistivity by the photogenerated carriers (Fig. 4e and f). The flexible and transparent polymer architecture of the PD empowered a stable device performance after 1000 bending cycles and photosensitivity at 360 degrees of illumination (Fig. 4j). The self-powered PD exhibited an impressive maximum voltage responsivity of 79.4 V mW<sup>-1</sup> cm<sup>-2</sup> and a  $\sim 90\%$  change in voltage at an incident light intensity of 100 mW cm<sup>-2</sup> compared to the voltage obtained in dark.

#### 1.5 Common strategies to enhance the figures of merit of OLHP PDs

Table 2 summarizes a representative list of OLHP based PDs where various strategies such as crystal structure engineering, modulation of the synthesis procedure, and broadening of the spectral range were employed to enhance device characteristics.

**1.5.1 Crystallite structure engineering.** Several attempts have been made to improve the figures of merit for the perovskite based self-powered PDs by engineering the crystallite structure and composition. Perovskite single-crystal materials exhibit high carrier mobility ( $>100$  cm<sup>2</sup> V<sup>-1</sup> s<sup>-1</sup>), long diffusion lengths, low trap-state densities ( $\sim 10^{10}$  cm<sup>-3</sup>), and high absorption coefficients as compared to their polycrystalline counterparts which are beneficial for the realization of high-performance PDs.<sup>91</sup> Fang *et al.* published a pioneering report on single crystal based planar PD driven by a drum shaped assembly of two DVDs functioning as a triboelectric nanogenerator.<sup>92</sup> The nano-patterned polycarbonate substrate face of DVD was used as one of the friction layers of the TENG. An Al conductive tape was applied on the reverse side of the DVD to serve as an electrode. A sanded Cu conductive tape pasted on another DVD acted as the opposite friction layer. Multiple pieces of polyethylene terephthalate (PET) were used to connect the two friction layers face-to-face, resulting in a drum shaped TENG with the single crystal perovskite sandwiched in between. Fig. 5a represents the



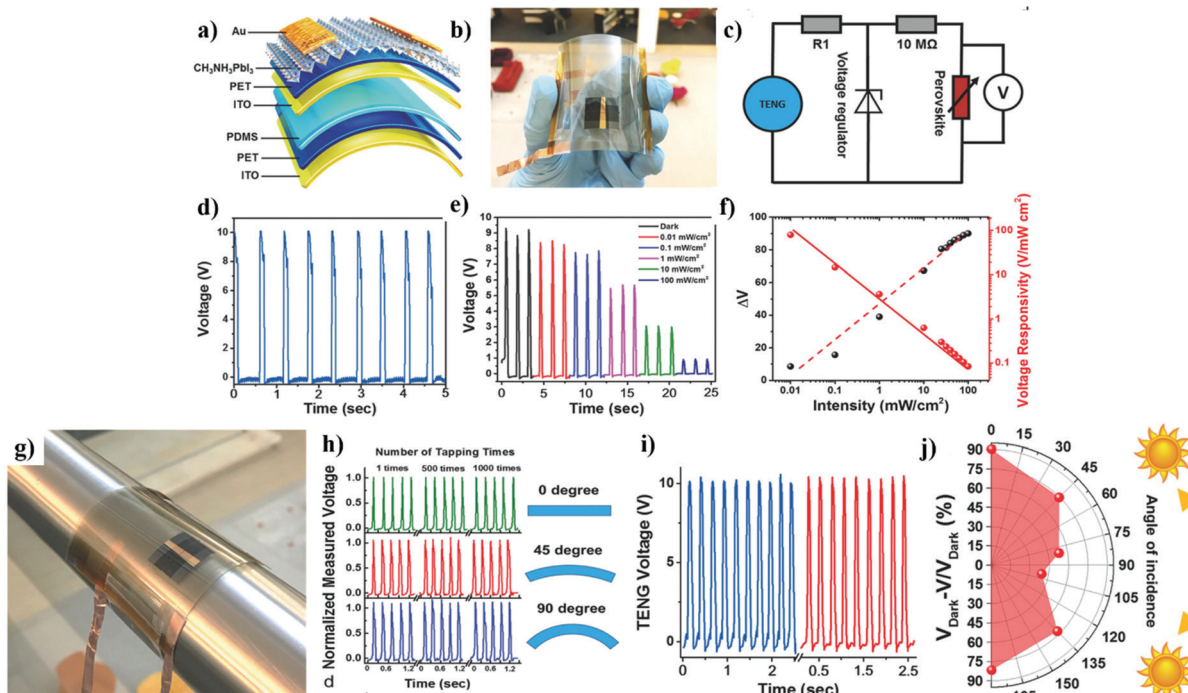


**Fig. 4** Device structure, optical image, circuit diagram, and electro-optical measurements of the TENG powered flexible PD: (a) schematic illustration of the self-powered flexible PD. (b) Optical image demonstrating high transparency and flexibility of the as-fabricated OLHP PD. (c) Equivalent circuit diagram. (d) Regulated voltage output of the TENG driven by finger tapping, corresponding to voltage spikes. (e) Light intensity dependent voltage response of the PD. (f) The change in the measured voltage ( $\Delta V$ ) and voltage responsivity of the device at different light intensities. (g) Photograph of a perovskite PD attached to a curved surface. (h) The self-powered perovskite PD features stable performance upon repeated bending at various angles of curvature. (i) The TENG output by two different people, demonstrating the highly regulated TENG voltage output attributing to the regulating circuit. (j) Change in voltage response at various angles of incident light. Reproduced with permission from Leung *et al.*, *Adv. Mater.*, **30**, 1704611.<sup>90</sup> © 2018 WILEY-VCH Verlag GmbH & Co. KGaA, Weinheim.

equivalent circuit of the self-powered PD system in which OLHP single crystal served as a TENG. The self-powered device yielded up to 200 V and 55 mA upon being subjected to finger tapping (Fig. 5b and c). The crude yet simplistic approach enabled large responsivity of  $196 \text{ V (mW cm}^{-2}\text{)}^{-1}$  with a wide detection range from 10 to 100  $\text{mW cm}^{-2}$  (Fig. 5d–f). Capitalizing on the advantage of higher current saturation density offered by asymmetric metal contacts (Au-Al), Ding *et al.* fabricated a facile Schottky junction (Au/CH<sub>3</sub>NH<sub>3</sub>PbI<sub>3</sub>/Al) enabled PD with an inherent built-in field.<sup>93</sup> The single crystal MAPbI<sub>3</sub> device exhibited responsivity as high as  $0.24 \text{ A W}^{-1}$  and a fast rise time and decay time of 71  $\mu\text{s}$  and 112  $\mu\text{s}$ , respectively. Cao *et al.* fabricated a MAPbBr<sub>3</sub>/MAPbI<sub>x</sub>Br<sub>3-x</sub> core–shell heterojunction-based PD.<sup>94</sup> The strong local electric field arising from band bending at the MAPbBr<sub>3</sub>/MAPbI<sub>x</sub>Br<sub>3-x</sub> heterojunction facilitated efficient exciton dissociation and suppressed charge recombination. Under the influence of the inherent field, the electrons were injected into the CH<sub>3</sub>NH<sub>3</sub>PbI<sub>x</sub>Br<sub>3-x</sub> shell while the holes were transferred to the MAPbBr<sub>3</sub> single crystal core, enabling photoresponse at zero bias. The self-powered PD exhibited a responsivity of  $11.5 \text{ mA W}^{-1}$  and a quantum efficiency of 3.17%, both being higher than the respective values observed for the MAPbBr<sub>3</sub> single crystal counterpart. Despite the advantages offered by single crystals, fabricating solution processed large-area single crystal films with controllable thickness is still a major challenge. Pan *et al.* instead proposed utilization of perovskite microcrystals (MCs) that possess advantages similar to

single crystal perovskite (low defect state density and high carrier mobility) with the ability of tuning film thickness by tweaking precursor solution concentration and antisolvent content.<sup>95</sup> The authors fabricated a HTL-free ITO/SnO<sub>2</sub>/MAPb(I<sub>x</sub>Br<sub>1-x</sub>)<sub>3</sub> MC film/carbon heterojunction assembly with adjustable band gap and the ability to operate without external bias. With the decrease in the iodide content (x) in the perovskite precursor solution, the absorption edge of the MAPb(I<sub>x</sub>Br<sub>1-x</sub>)<sub>3</sub> MC film gradually shifted to the blue region with the corresponding bandgap increasing from 1.53 eV of MAPbI<sub>3</sub> to 2.22 eV of MAPbBr<sub>3</sub>. The perovskite MC films with optimized thickness led to an on/off ratio of  $2 \times 10^5$ , a responsivity of  $0.26 \text{ A W}^{-1}$ , a specific detectivity of  $7.01 \times 10^{11}$  Jones, a rise/fall time of 80/580 ms, and a linear dynamic range of 107 dB. Furthermore, the MC based PDs show negligible attenuation upon continuous exposure to light and air for 30 minutes and an overall 16% decrease in performance when stored in air for a month. In a recent work, Perumal *et al.* presented an ultrasonication based ligand-assisted reprecipitation (LARP) technique to produce air-stable MAPbI<sub>3</sub> nanocrystals. The MAPbI<sub>3</sub> nanocrystals were spray-casted or drop-casted over patterned asymmetric ITO-Ag electrodes to obtain a self-powered PD.<sup>96</sup> The optimized PD showed a responsivity of  $1.42 \text{ A W}^{-1}$  and a specific detectivity of  $1.77 \times 10^{13}$  Jones under an 808 nm light illumination at zero bias, and maintained 90% performance over 1 month.

**1.5.2 Synthesis strategy.** The quality and compactness of the perovskite film strongly determine its inherent stability and

Table 2 Summary of OLHP based self-driven PDs where various strategies were utilized to improve the key device characteristics

Strategy	Device architecture	Self-powered operating principle	Operating wavelength	Responsivity	Detectivity (Jones)	Light switching ratio	Response speed (rise/fall time)	Ref.
Crystallite structure engineering	Al/CH <sub>3</sub> NH <sub>3</sub> PbI <sub>3</sub> /Cu	Triboelectricity	white light	196 V (mW cm <sup>-2</sup> ) <sup>-1</sup>			<0.2/<0.2 s (4 V)	92
	Au/CH <sub>3</sub> NH <sub>3</sub> PbI <sub>3</sub> /Al	Schottky junction	808 nm	0.24 A W <sup>-1</sup>		20	71/112 $\mu$ s	93
	FTO/MAPbBr <sub>3</sub> /MAPbI <sub>x</sub> Br <sub>3-x</sub> /Au	Heterojunction	450 nm	11.5 mA W <sup>-1</sup>			2.3/2.76 s	94
	ITO/SnO <sub>2</sub> /MAPb(I <sub>x</sub> Br <sub>1-x</sub> ) <sub>3</sub> /MC/C	Heterojunction		0.26 A W <sup>-1</sup>	7.01 $\times$ 10 <sup>11</sup>	2 $\times$ 10 <sup>5</sup>	80/580 $\mu$ s	95
	ITO/MAPbI <sub>3</sub> NCS/Ag	Schottky junction	808 nm	1.42 A W <sup>-1</sup>	1.77 $\times$ 10 <sup>13</sup>	932	279/341 ms	96
	FTO/TiO <sub>2</sub> /CH <sub>3</sub> NH <sub>3</sub> PbI <sub>3</sub> /Spiro-OMeTAD/Ag	Heterojunction	650 nm	0.55 A W <sup>-1</sup>	$\sim$ 10 <sup>12</sup>	$\sim$ 10 <sup>4</sup>	460/940 ns	97
	FTO/TiO <sub>2</sub> /Cs <sub>0.05</sub> FA <sub>0.16</sub> -MA <sub>0.79</sub> PbI <sub>2.7</sub> Br <sub>0.3</sub> /Spiro-OMeTAD/Ag	Heterojunction					1.73 $\times$ 10 <sup>3</sup>	12.4/26.4 $\mu$ s
	FTO/NiO <sub>x</sub> /MAPbI <sub>3-x</sub> Cl <sub>x</sub> //PCBM/Au	Heterojunction	632 nm	112.9 A W <sup>-1</sup>	3.53 $\times$ 10 <sup>14</sup>		0.23/0.38 s	99
	FTO/TiO <sub>2</sub> /MAPbI <sub>3-x</sub> Br <sub>x</sub> //PCBM/Au	Heterojunction	632 nm	45 A W <sup>-1</sup>	1.15 $\times$ 10 <sup>14</sup>		0.24/0.38 s	100
	FTO/TiO <sub>2</sub> /CH <sub>3</sub> NH <sub>3</sub> Pb <sub>0.99</sub> Bi <sub>0.01</sub> I <sub>3</sub> /Au	Heterojunction	Visible light	1 $\times$ 10 <sup>-4</sup> A W <sup>-1</sup>			902/762 ms	101
Modulation of synthesis procedure	ITO/PEDOT:PSS/(FASnI <sub>3</sub> ) <sub>0.6</sub> -(MAPbI <sub>3</sub> ) <sub>0.4</sub> /C <sub>60</sub> /BCP/Ag	Heterojunction	900 nm	0.4 A W <sup>-1</sup> (-0.2 V)	1.1 $\times$ 10 <sup>12</sup> (-0.2 V)		6.9/9.1 $\mu$ s	103
	Si/MPS/metal/MoO <sub>3</sub> /PEDOT:PSS/Sn-rich binary perovskite/PC <sub>61</sub> BM/ZrAcac/transparent thin metal film/MoO <sub>3</sub>	Heterojunction	940 nm	0.2 A W <sup>-1</sup>	$\sim$ 10 <sup>11</sup>		90 ns/2.27 $\mu$ s	104
	FTO/SnO <sub>2</sub> /KMAPbCl <sub>x</sub> Br <sub>3-x</sub> /Spiro-OMeTAD/Au	Heterojunction					$\sim$ 71 ns	105
Spectral range broadening	MAPbI <sub>3-x</sub> Cl <sub>x</sub> /TiO <sub>2</sub> /Si	Heterojunction	800 nm	870 mA W <sup>-1</sup> (+4 V)	6 $\times$ 10 <sup>12</sup> (+4 V)	116	50/150 ms	106

overall device performance. Developing and improvising fabrication techniques that allow precise control over the quality, morphology, composition, and crystallinity of the perovskite films are thus crucial. Tong *et al.* explored a lower temperature range of 90–150 °C and a fast chemical vapor

deposition (LF-CVD) route to synthesize compact uniform and smooth perovskite films.<sup>97</sup> The expansive gas–solid reaction of perovskite crystallites with optimal annealing at 120 °C for 30 min led to the restriction of pinholes to grain boundaries while maintaining the integrity of the thin film. Simultaneously,

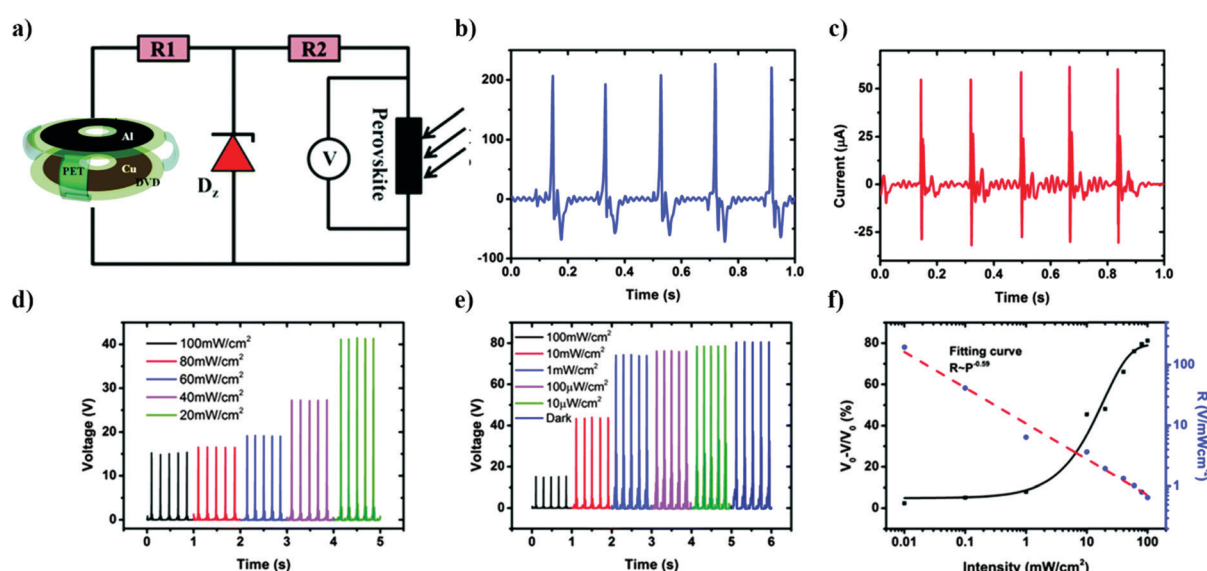


Fig. 5 Circuit diagram and optoelectronic characteristics of the triboelectric effect driven MAPbI<sub>3</sub> single crystal PD: (a) the equivalent circuit of the self-powered PD nanosystem where  $D_z$  represents a commercial Zener diode. Measured (b)  $V_{oc}$  and (c)  $I_{sc}$  response from the TENG during the periodical finger tapping in the forward connection. The measured voltage drop across the CH<sub>3</sub>NH<sub>3</sub>PbI<sub>3</sub> single crystal photodetector in (d) dark and under (e) various illumination intensities. (f) Voltage change (defined as  $(V_0 - V)/V_0$ ) and photoresponsivity of the nanosystem as a function of illumination intensity. Reproduced from ref. 92 with permission from The Royal Society of Chemistry.

the accumulated strain at the colliding grain boundary interfaces led to selective evaporation of MAI leaving behind a thin layer of  $\text{PbI}_2$  at the grain boundaries. The authors claimed that the wider bandgap of  $\text{PbI}_2$  in comparison to perovskite provided good passivation at the grain boundaries and helped reduce local recombination centres and block local leakage current. The corresponding self-driven vertically configured FTO/TiO<sub>2</sub>/perovskite/Spiro-OMeTAD/Ag PD device exhibited a detectivity of  $\sim 10^{12}$  Jones, a responsivity of  $0.55 \text{ A W}^{-1}$  with fast rise time and fall time of 460 ns and 640 ns, respectively (Fig. 6). The two-month air-stable PD also showcased a wide 3 dB bandwidth up to 0.9 MHz. Adams *et al.* proposed to alleviate the repeatability and scalability challenges associated with the typical anti-solvent drip method used in the synthesis of perovskite films by using the anti-solvent bath method with improvised annealing.<sup>98</sup> A low-temperature fabrication method was employed to obtain large grain sized, Cs/FA/MA triple cation perovskite PDs with a low dark current,  $> 10^3$  on/off ratio, and a rise time of 12.4  $\mu\text{s}$ . Pammi *et al.* fabricated high-quality large grain size rich polycrystalline thin films of  $\text{MAPbI}_3-x\text{Cl}_x$ <sup>99</sup> and  $\text{MAPbI}_3-x\text{Br}_x$ <sup>100</sup> via the chemical vapor deposition (CVD) method. The corresponding PDs exhibited an impressive figure of merit. More importantly, after 500 h of illumination, the normalized responsivity reduced by 25% and 29% for the  $\text{MAPbI}_3-x\text{Cl}_x$  and  $\text{MAPbI}_3-x\text{Br}_x$  based PDs, respectively, in comparison to 62% in pristine  $\text{MAPbI}_3$  based PD, signifying the enhanced stability of the chlorine and bromine doped perovskite films. Sadhasivam *et al.* used CVD to deposit a crystalline layer of  $\text{Pb}_{0.99}\text{Bi}_{0.01}\text{I}_2$  over TiO<sub>2</sub> nanoarrays which was later transformed to  $\text{CH}_3\text{NH}_3\text{Pb}_{0.99}\text{Bi}_{0.01}\text{I}_3$  by introducing methylamine iodide at distinct time intervals.<sup>101</sup> The corresponding PD exhibited a responsivity of  $10^{-4} \text{ A W}^{-1}$  at 0 V.

**1.5.3 Broadening of the PD spectral range.** One of the limitations associated with perovskite-based PDs is their attenuated absorption capacity in the NIR range. To broaden the spectral range of the perovskite-based PDs, two approaches have been commonly adopted: (1) lowering the bandgap of perovskite by substituting cation or/and a halide moiety<sup>102</sup> or (2) combining the perovskite layer with another narrow bandgap semiconductor. Wang *et al.* followed the first strategy of cation and halide substitution to fabricate a low bandgap ( $\text{FASnI}_3$ )<sub>0.6</sub> ( $\text{MAPbI}_3$ )<sub>0.4</sub> perovskite-based PD with a broadband response extending from UV (300 nm) to NIR (1000 nm).<sup>103</sup> The as-fabricated vertically configured ITO/PEDOT:PSS/( $\text{FASnI}_3$ )<sub>0.6</sub> ( $\text{MAPbI}_3$ )<sub>0.4</sub>/C<sub>60</sub>/BCP/Ag device exhibited almost identical EQE spectra under 0 and  $-0.2$  V, indicating its self-powered ability. The authors used C<sub>60</sub> as a hole blocking layer and to passivate the surface charge traps, leading to a reduced leakage current under reverse bias. The thin BCP layer served as a cathode buffer layer to enhance the contact between the C<sub>60</sub> layer and the Ag cathode. Zhu *et al.* illustrated a room-temperature strategy to manipulate the crystallization kinetics of Sn-rich binary perovskite films fabricated over a complementary metal-oxide-semiconductor (CMOS) compatible silicon substrate.<sup>104</sup> The Pb-Sn mixed perovskites are considered promising narrow-bandgap materials offering the advantage of expanding the spectral response to the NIR region. However, compared to their Pb analogues, Sn-based perovskite precursors have a greater tendency to react and crystallize at room temperature, resulting in high surface roughness and severe pinholes in the corresponding films. By carrying out careful experimental and theoretical studies focused primarily on the timespan between the antisolvent washing process and the post-annealing

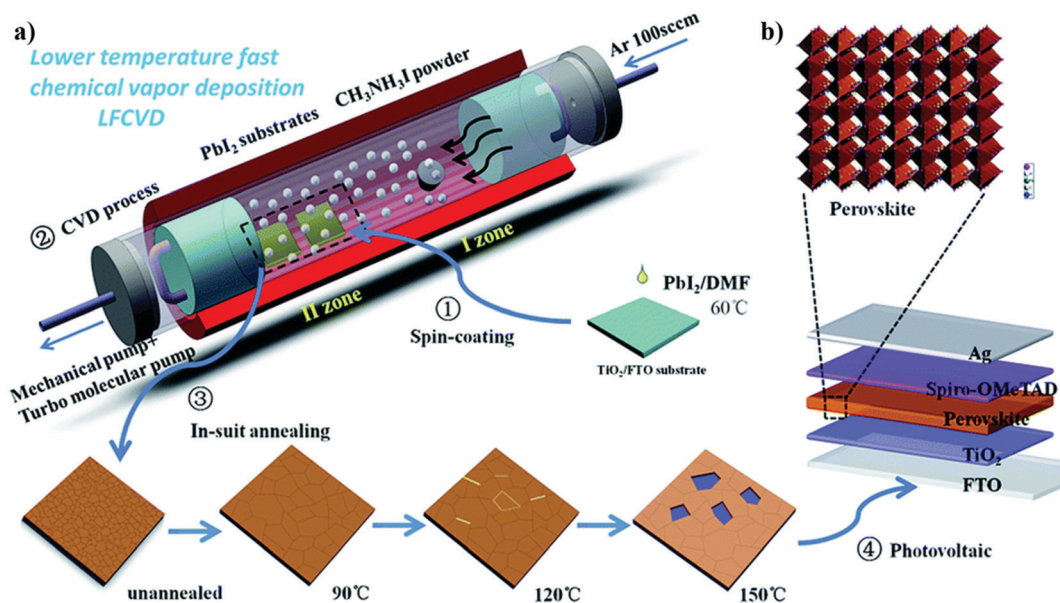


Fig. 6 Stepwise CVD fabrication process and multilayer structure of the perovskite device: (a) schematic illustration of the configuration of the two-temperature-zones furnace tube and the fabrication procedure of a lower temperature fast chemical vapor deposition process (LF-CVD) for synthesizing perovskite films. (b) The multilayer structure of the final perovskite photovoltaic detector. Reproduced from ref. 97 with permission from The Royal Society of Chemistry.



treatment, the authors were able to control the density and location of the compact nanocrystals formed in the precursor films. Upon flash annealing, these compact nanocrystals coalesced into a smooth pin-hole free  $\text{MASn}_x\text{Pb}_{1-x}\text{I}_3$  film with preferred orientation and reduced trap density. The corresponding self-powered devices with a carrier extraction layer/metal/Si substrate structure, achieved a high responsivity of  $0.2 \text{ A W}^{-1}$  at 940 nm, a large linear dynamic range of 100 dB, and a fast fall time of  $2.27 \mu\text{s}$ . The authors also demonstrated a  $6 \times 6$ -pixel array based on the Sn rich binary perovskite films with excellent photocurrent uniformity. In another interesting work aimed at producing filter-free/spectrum sensitive PD, as illustrated in Fig. 7a, Sun *et al.* demonstrated *in situ* bandgap gradient within an array of  $\text{KMAPbCl}_x\text{Br}_{2-x}$  absorber films when subjected to a temperature bridge across the integrated device.<sup>105</sup> The integrated self-driven PD with a high spectral resolution ( $\sim 80 \text{ nm}$ ) (Fig. 7b and c) exhibited a rapid response time ( $\sim 71 \text{ ns}$ ) due to the influence of

carrier concentration ( $\text{Cl}^-$  vacancies) over interfacial capacitance while maintaining a maximum external quantum efficiency (EQE) of over 90%. Fig. 7d represents the schematic layout of the  $\text{KMAPbCl}_x\text{Br}_{3-x}$  film-based spectrum detection system. On the other hand, following the second approach for enhancing the spectral response of perovskite-based PDs, Cao *et al.* combined a narrow bandgap n-Si wafer with an active layer of  $\text{MAPbI}_3$ , spin-coated over a  $\text{TiO}_2$  interlayer to fabricate a trilayer hybrid PD.<sup>106</sup> The  $\text{TiO}_2$  thickness dependent *I-V* rectification characteristics suggested the presence of a built-in electric field in the as-prepared PD and its ability to work under zero bias. Showcasing a broad spectral response up to 1150 nm, the PD exhibited a rise time and decay time of 50 and 150 ms, respectively.

### 1.6 Flexible PDs

Compared with the traditional devices based on a rigid silicon substrate, flexible PDs have wider applications in the field of

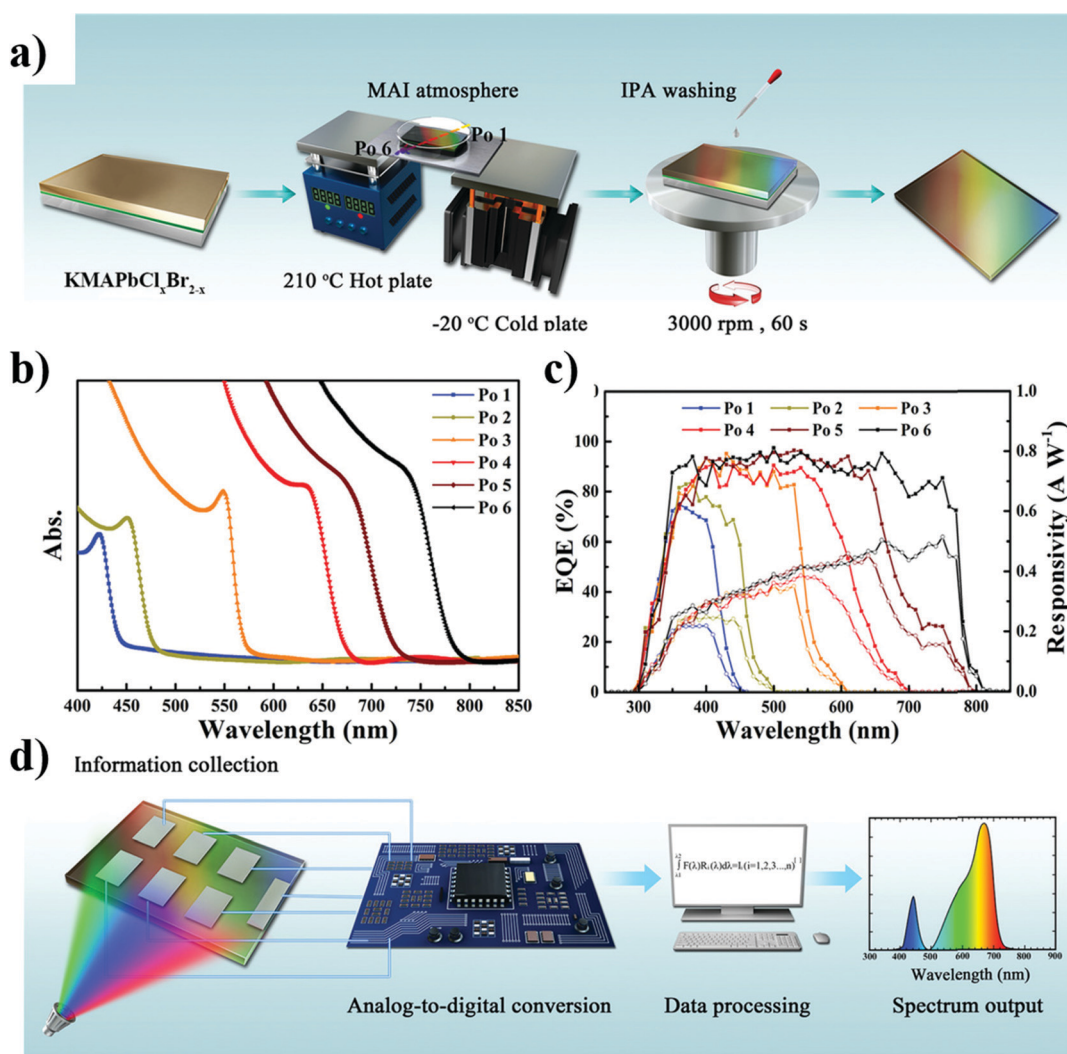


Fig. 7 Fabrication procedure and optical and electro-optical measurements of gradient perovskite film: (a) schematic diagram of the gradient perovskite absorber preparation process. (b) The absorption spectra of the gradient perovskite absorber with different positions. (c) The EQE spectra of the PD based on various absorber positions. (d) Schematic diagram of the final color/spectrum detection system. Reproduced with permission from Sun *et al.*, *Adv. Mater.*, **32**, 1908108.<sup>105</sup> © 2020 WILEY-VCH Verlag GmbH & Co. KGaA, Weinheim.



wearable and portable devices owing to their reduced weight and promising applications in healthcare, robotics, epidermal sensing, and so forth. Due to their low-temperature solution-processing and light absorption characteristics, perovskite thin films can serve as an optimal light-harvesting material in such applications. Among the initial works based on OLHP flexible PDs, Bao *et al.* demonstrated a flexible PD with poly(ethylene 2,6-naphthalate) (PEN)/Au NW serving as a transparent electrode.<sup>107</sup> The peak EQE and responsivity of the device reached 60% and 314 mA W<sup>-1</sup>, respectively, with a 4.0  $\mu$ s rise time and a 3.3  $\mu$ s fall time. In another work, Sun *et al.* utilized a blend of  $\text{CH}_3\text{NH}_3\text{PbI}_3$  and Spiro-OMeTAD as a photosensitive material over low-cost carbon cloth, serving both as a substrate and a conducting electrode to fabricate a flexible PD.<sup>108</sup> The solution processed device exhibited high detectivity and light responsivity, a large on/off ratio, and a broad-spectrum response to light ranging from UV (300 nm) to NIR (820 nm) at zero bias. The flexible PD exhibited a fast response speed and reproducible characteristics under white light irradiation after 80 bending cycles and showed photoresponse even at high bending angles such as 180°. The same group later reported a flexible PD based on a single fibre. Here, perovskite microcrystals were solution coated over a commercial carbon fibre with an intermediated thin layer of  $\text{TiO}_2$ .<sup>109</sup> A CuO nanowire– $\text{Cu}_2\text{O}$  compact layer grown over a flexible Cu fibre was double twisted over the perovskite-coated carbon fibre to function as a cathode while the carbon tape end of the parent fibre was utilized as an anode Fig. 8a represents the complete fabrication process and energy level diagram of the as-fabricated fibre PD. Under the self-powered mode, the flexible PD exhibited ultralow dark current ( $10^{-11}$  A) empowering high detectivity of up to  $10^{13}$  Jones while the narrow bandgap of CuO enabled the broadening of the spectral response range from UV (350 nm) to NIR (1050 nm) (Fig. 8b–e). The device demonstrated a rapid response speed

(<200 ms) and reproducible photoresponse characteristics after being subjected to 60 bending cycles. Another similar work reporting a flexible wire-shaped PD is from Adams *et al.*<sup>110</sup> The research emphasized the predominance of Joule heating (direct conversion of electric energy to heat) over the conventional hot-plate heating method by allowing rapid heating or cooling of a substrate and thereby enabling a higher degree of control. The ohmic heating method allowed uniform temperature distribution across the thread-like carbon nanotube yarn (CNY) which, in turn, facilitated the deposition of a compact polycrystalline perovskite layer. The asymmetric top InGa and bottom CNY electrode contacts created a built-in potential sufficient to overcome the binding energy of photogenerated electron–hole pairs. The resultant PD had a responsivity of 10.2 A W<sup>-1</sup> and a detectivity of  $1.76 \times 10^{11}$  Jones with an on/off ratio of 45. Utilizing the anti-solvent crystallization technique, Lim *et al.* patterned an array of  $\text{MAPbI}_3$  nanoribbons over a variety of substrates including the flexible polyimide substrate.<sup>111</sup> Dripping of nonpolar toluene facilitated the abrupt precipitation of perovskite grains and removal of residual perovskite precursor solvent confined within the hydrophobic trap of polymethyl methacrylate (PMMA) nanotemplate, leading to a directional growth of perovskite grains. The phase switching local hysteresis and amplitude butterfly loops, suggestive of the ferroelectric nature of  $\text{MAPbI}_3$ , were observed during the characterization of the perovskite films. The authors hence argued that the ferroelectricity and anisotropic alignment of the hierarchical array of  $\text{MAPbI}_3$  nanoribbons led to the self-powered and polarization-sensitive optoelectronic response in the resultant flexible PD. One of the major challenges against the realization of optimum capabilities of the perovskite-based flexible PDs lies in the high-temperature treatment required for the carrier extraction layer during device fabrication. Wang *et al.* in their work focussed on low temperature (80 °C) processed  $\text{In}_2\text{S}_3$  nanoflake film grown to

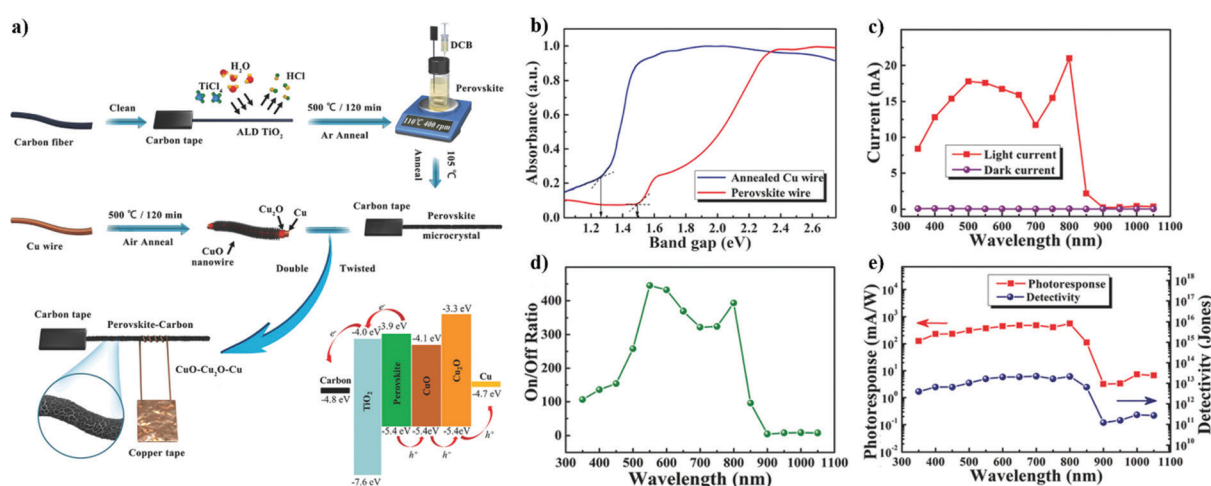


Fig. 8 Fabrication strategy and the electro-optical response of the perovskite-based fiber-shaped PD: (a) schematic illustration of the fabrication process and energy level diagram of the fiber-shaped PD. (b) Absorption spectrum of perovskite–carbon fiber and CuO– $\text{Cu}_2\text{O}$ –Cu wire with the corresponding fitted bandgap. (c) Photocurrent and dark current, (d) calculated on/off ratio, and (e) spectroscopic photoresponse and detectivity under light illumination of varying wavelengths (350–1050 nm). Reproduced with permission from Sun *et al.*, *Adv. Mater.*, **30**, 1706986.<sup>109</sup> © 2018 WILEY-VCH Verlag GmbH & Co. KGaA, Weinheim.



effectively serve as the electron transport and hole blocking layer over the ITO/PEN substrate with  $\text{MAPbI}_3$  serving as a photosensitive layer.<sup>112</sup> The resultant PD exhibited a broadband response up to the NIR range with responsivity up to  $451 \text{ mA W}^{-1}$  at 720 nm without any external power supply. The flexible device showed only a 15% loss of current with a bending radius up to 2.5 mm. Tian *et al.* demonstrated a relatively less researched, nested inverse opal structured  $(\text{Cs}_{0.05}(\text{FA}_{0.85}\text{MA}_{0.15})_{0.95}\text{Pb}(\text{I}_{0.85}\text{Br}_{0.15})_3)$  perovskite-based flexible PD.<sup>113</sup> The combined effect of improved light trapping and perovskite crystallinity enabled the self-driven device to exhibit a responsivity of  $473 \text{ mA W}^{-1}$  and a detectivity of  $1.35 \times 10^{13}$  Jones with reproducible photoresponse after 500 bending cycles. The PS template-assisted device fabrication enabled enhanced hydrophobicity across the device surface which in turn permitted the PD stored in an ambient environment to operate for over 16 days without significant decay in performance. Several other reports have appeared recently representing the increased attention being paid to flexible PDs. Shin *et al.* reported photodiode cum solar cell with identical configuration (TETRA-GR/MoS<sub>2</sub>/MAPbI<sub>3</sub>/PCBM/BCP/Al) utilizing bilayer MoS<sub>2</sub> as the ETL and triethylenetetramine doped graphene (TETA-GR) as a transparent conductive electrode.<sup>114</sup> The flexible PD maintained about 80% of its original responsivity even after 1000 bending tests at a radius of curvature of 4 mm. Later, the authors showcased the versatility of MoS<sub>2</sub> by utilizing it instead as the HTL in a similar bifunctional flexible device but with an inverted p-i-n configuration.<sup>115</sup> The flexible PD maintained  $\sim 57\%$  of its initial photocurrent after 3000 bending cycles at a curvature radius of 4 mm. More recently, Tao *et al.* demonstrated  $\text{CH}_3\text{NH}_3\text{PbI}_3$  NWs sandwiched between asymmetric Ni-Al electrodes on a flexible polyimide film.<sup>116</sup> The formation of the metal/perovskite Schottky barrier at the interface of asymmetric Al (4.3 eV) and Ni (5.1 eV) electrodes led to a built-in electric field in the device which could effectively separate charge carriers. The corresponding self-powered device exhibited a responsivity of  $0.227 \text{ A cm}^{-2}$  at an incident light power of  $1 \times 10^{-8} \text{ W cm}^{-2}$  and an on/off ratio of 147. Although appreciable developments have been made in the field of flexible self-powered PDs, it is worth considering that most of the reported PDs have small active areas and their optimum performance lasts only for few thousand cycles. Hence, besides optimizing the photosensitive perovskite layer to mitigate material degradation issues, a careful selection of suitable electrodes and substrates to facilitate

large-area self-powered PDs with a stable long-term device operation is equally critical. In a recent work, Saraf *et. al* utilized Au-Pt gold nanoparticle chain-based electrodes on a flexible filter membrane to fabricate a porous Au-Pt/PS-MAPbI<sub>3</sub>/Au-Pt PD assembly.<sup>117</sup> The flexible PD maintained 85% of its initial performance after 10 000 bending cycles at  $120^\circ$ . The highly flexible nanoparticle chain electrodes can potentially be expanded to fabricate asymmetric contact to induce a built in electric field within the perovskite and obtain a self-powered PD. The key figures of merit and device configuration of OLHP based flexible PDs are presented in Table 3.

## 2. Supercapacitors

Photovoltaic cells have the limitation of unstable power output due to fluctuations in sunlight. Integration of energy storage devices with solar cells to store energy during sunlight and provide it under low light conditions can be used to power wearable electronics.<sup>118-126</sup> This provides a stable output power compared with that of a solar cell alone. Li *et al.* reported a flexible PSC driven photo-rechargeable lithium-ion capacitor (LIC) for strain sensors.<sup>127</sup> It achieved an overall efficiency of 8.41% with a high output voltage of 3 V at a discharge current density of  $0.1 \text{ A g}^{-1}$ . The photovoltaic unit was made by the deposition of OLHP on an ITO coated PET sheet in Ag/BCP/PCBM/MA<sub>1-y</sub>FA<sub>y</sub>PbI<sub>3-x</sub>Cl<sub>x</sub>/NiO<sub>x</sub>/ITO/PET configuration. A single cell reached a corresponding PCE of 14.01%,  $V_{oc}$  of 1.05 V, short-circuit current density ( $J_{sc}$ ) of  $18.71 \text{ mA cm}^{-2}$ , and fill factor (FF) of 0.71. Researchers combined four of these PSCs to provide 3.95 V with 10.2% efficiency under AM 1.5G solar irradiation. The LIC could be charged to 3 V in 20 min with a charge current of 1.22 mA. As observed in Fig. 9a-c, the wearable device was able to monitor finger motion and pulsation continuously and precisely, without an external power source. In a separate work, Du *et al.* integrated a flexible graphene-based supercapacitor and a perovskite based solar cell to fabricate a self-powered device.<sup>128</sup> The configuration of the perovskite hybrid solar cell (pero-HSC) was ITO/PEDOT:PSS/CH<sub>3</sub>NH<sub>3</sub>PbI<sub>3-x</sub>Cl<sub>x</sub>/PC<sub>61</sub>BM/Al. Under AM 1.5G illumination, the pero-HSC exhibited a PCE of 14.13%, a  $V_{oc}$  of 0.90 V, a  $J_{sc}$  of  $22.59 \text{ mA cm}^{-2}$ , and an FF of 0.695. The supercapacitor was charged to 0.75 V via the solar cell and

Table 3 Summary of OLHP based flexible self-powered PDs and their associated device characteristics

Device architecture	Self-powered operating principle	Operating wavelength	Responsivity	Detectivity (Jones)	Light switching ratio	Response speed (rise/fall time)	Ref.
Al/MAPbI <sub>3</sub> /Cu between pair of PET film	Triboelectricity						107
C/TiO <sub>2</sub> /MAPbI <sub>3</sub> -Spiro-OMeTAD/Au	Heterojunction	750 nm	$16.9 \text{ mA W}^{-1}$	$1.10 \times 10^{10}$	69.1	<200/<200 ms	108
C/TiO <sub>2</sub> /MAPbI <sub>3</sub> /CuO/Cu <sub>2</sub> O/Cu	Heterojunction	800 nm	$562.9 \text{ mA W}^{-1}$	$2.15 \times 10^{13}$	393	<200 ms	109
CNY/CH <sub>3</sub> NH <sub>3</sub> PbI <sub>3</sub> /In/Ag	Heterojunction	617 nm	$10.2 \text{ A W}^{-1}$	$1.76 \times 10^{11}$	45	0.393/0.132 s	110
Au/MAPbI <sub>3</sub> /Au on polyimide	Heterojunction	300 nm	$2.2 \text{ mA W}^{-1}$	$1.76 \times 10^{11}$		27.2/26.2 ms (2 V)	111
PEN/ITO/In <sub>2</sub> S <sub>3</sub> /MAPbI <sub>3</sub> /Spiro-OMeTAD/Ag	Heterojunction	720 nm	$451 \text{ mA W}^{-1}$	$1.1 \times 10^{11}$ (+0.5 V)		<200/<200 ms	112
PEN/ITO/SnO <sub>2</sub> /MAPbI <sub>3</sub> /Spiro-OMeTAD/Ag	Heterojunction	720 nm	$473 \text{ mA W}^{-1}$	$1.35 \times 10^{13}$		0.35/0.18 ms	113
PET/TETRA-GR/MoS <sub>2</sub> /MAPbI <sub>3</sub> /PTAA/Al	Heterojunction	720 nm	$0.40 \text{ A W}^{-1}$	$5.0 \times 10^9$		1.63/0.98 $\mu$ s	114
PET/co-GR/MoS <sub>2</sub> /MAPbI <sub>3</sub> /PCBM/BCP/Al	Heterojunction	700 nm	$410 \text{ mA W}^{-1}$	$7.99 \times 10^{10}$	136 110	0.7-0.9/0.4-0.6 s	115
Ni/MAPbI <sub>3</sub> NWs/Al on polyimide film	Schottky Junction	532 nm	$0.227 \text{ A cm}^{-2}$	$1.36 \times 10^{13}$	147	61/42 ms	116



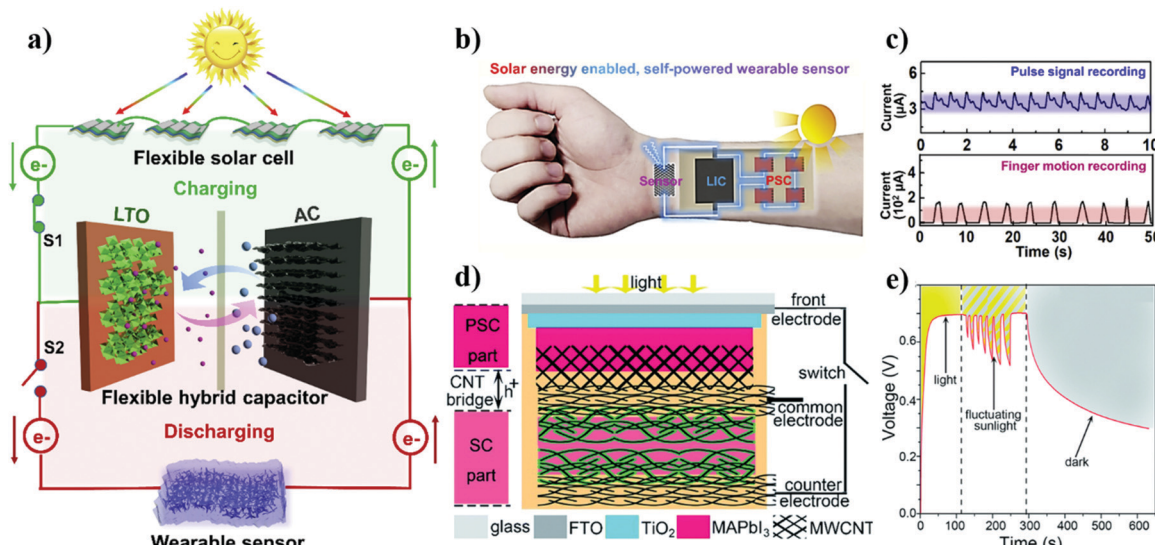


**Fig. 9** Schematic of the perovskite photovoltaic cell powered supercapacitor and photocapacitor and their respective responses: (a) scheme of the flexible PSC–LIC–sensor system. (b) Scheme of wearable PSC–LIC–sensor integrated system. (c) The output current response of pulse signal (upper panel) and finger motion (lower panel) under light illumination. Reprinted from Li *et al.*, flexible perovskite solar cell-driven photo-rechargeable lithium-ion capacitor for self-powered wearable strain sensors, *Nano Energy*, **60**, 247–56.<sup>127</sup> Copyright 2019, with permission from Elsevier. (d) Scheme of the photocapacitor made by organometal halide perovskite and PANI/CNT composites integrated using a CNT bridge. (e) The performance of a photocapacitor under different illumination conditions. Reproduced from ref. 129 with permission from The Royal Society of Chemistry.

discharged from 0.75 to 0 V at 1 A g<sup>-1</sup> in about 45 s, showing promising potential for utilization in self-powered portable and wearable personal devices. Liu *et al.* designed a photocapacitor with an overall energy storage efficiency of 70.9% by using carbon nanotubes (CNTs) as a bridge between self-powered organometal halide PSCs and supercapacitors to improve the overall performance.<sup>129</sup> As observed in Fig. 9d, the CNTs acted as a pathway for holes and electrons resulting in a smaller resistance. Under AM 1.5G simulated sunlight, the PSC of MAPbI<sub>3</sub> based solar cell achieved a PCE of 2.47%, a *V*<sub>oc</sub> of 0.7 V, a *J*<sub>sc</sub> of 9.2 mA cm<sup>-2</sup>, and an FF of 38%. The photocapacitor could be charged to 0.7 V in about 80 s. Following this, it slowly discharged from 0.7 V to 0.3 V, lasting for more than 300 s in dark, representing a more stable output than bare solar cells as illustrated in Fig. 9e.

### 3. Internet of things (IoT) sensors

Combining photovoltaic cells with the low-power radio frequency (RF) backscatter-based IoT sensors is a new approach to ubiquitous sensing for indoor applications.<sup>130–134</sup> The perovskite based photovoltaics can provide the necessary low power for these sensors enabling their operation for a long time. Kantareddy *et al.* reported a self-powered perovskite wireless temperature sensor with a 4 meter communication range.<sup>131</sup> Under 1 sun illumination, the PSC with the configuration of FTO/TiO<sub>2</sub>/(Rb<sub>0.01</sub>Cs<sub>0.05</sub>(FA<sub>0.83</sub>MA<sub>0.17</sub>)<sub>0.94</sub>Pb(I<sub>0.83</sub>Br<sub>0.17</sub>)<sub>3</sub>)/Spiro-OMeTAD/Au exhibited a *V*<sub>oc</sub> of 4.3 V, a *J*<sub>sc</sub> of 3.7 mA cm<sup>-2</sup>, an FF of 0.6, and a PCE of 10.1% with an active area of 1.06 cm<sup>2</sup>. This device was able to generate enough power to boot up a radio frequency identification (RFID) device that required 10–45 μW energy. Similarly, Mathews *et al.*

demonstrated an approach to integrate a wireless temperature sensor with PSCs acting as an external power source.<sup>132</sup> An integrated array of three photovoltaic cells, with the configuration of FTO/TiO<sub>2</sub>/(Rb<sub>0.01</sub>Cs<sub>0.05</sub>)(MA<sub>x</sub>FA<sub>1-x</sub>)<sub>0.94</sub>Pb(Br<sub>x</sub>I<sub>1-x</sub>)<sub>3</sub>/Spiro-OMeTAD/Au achieved a *V*<sub>oc</sub>, *J*<sub>sc</sub>, and PCE of 2.62 V, 46 μA cm<sup>-2</sup> and 13.2%, respectively. The output was 14.5 μW under a light intensity of 0.16 mW cm<sup>-2</sup> which is enough to power an RFID temperature sensor. The whole wireless temperature device was operational for over 8 h with regular measurements at 1.24 s intervals upon illumination by ambient light.

### 4. Transistors and photocatalysis

Photovoltaic devices have also been coupled with transistors<sup>74,135–139</sup> and electrochemical cells for degradation of organic pollutants,<sup>140,141</sup> due to their high *V*<sub>oc</sub> (0.9 V to 1.5 V) and power generation capacity. Jeong *et al.* reported a MAPbI<sub>3</sub> film coupled with PTAA, exhibiting a *J*<sub>sc</sub> and *V*<sub>oc</sub> of ~21 mA cm<sup>-2</sup> and ~1.08 V, respectively, with 18.3% PCE.<sup>135</sup> The *V*<sub>oc</sub> under red-LED could effectively gate the MoTe<sub>2</sub> field-effect transistors (FET) modulating the drain current (*I*<sub>D</sub>), which could turn on/off an OLED pixel (Fig. 10). Chen *et al.* reported that multi-walled CNTs and a methylamine (CH<sub>3</sub>NH<sub>2</sub>) modified perovskite achieved a PCE of 10.39%.<sup>140</sup> It was demonstrated that the CNT-incorporated MAPbI<sub>3</sub> perovskite thin film formed a smooth heterojunction structure, which facilitated the separation and transfer of charges. Also, CH<sub>3</sub>NH<sub>2</sub> could self-heal the perovskite surface while maintaining high crystallinity. This inhibited the charge recombination and improved the efficiency of the device. Thus, the CNT/CH<sub>3</sub>NH<sub>2</sub> perovskite exhibited a high *J*<sub>sc</sub> value of 22.02 mA cm<sup>-2</sup>. Combined with the CNT/TiO<sub>2</sub>

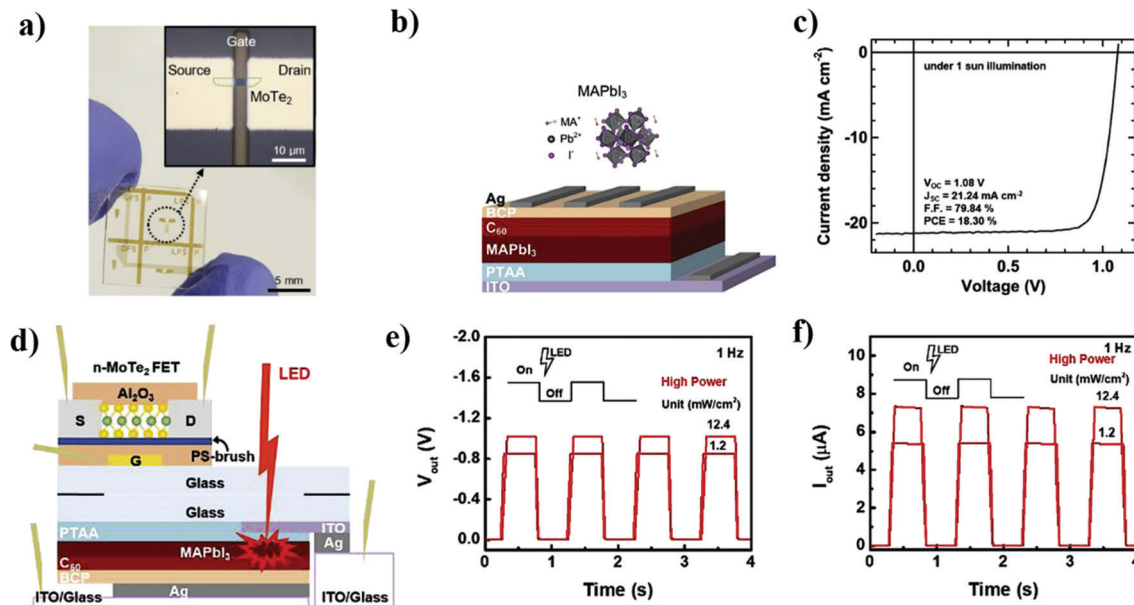


Fig. 10 Perovskite solar cell powered FET and the corresponding photosensitive response: (a) photo image and optical microscope image (inset) of n-MoTe<sub>2</sub> FET. (b) Scheme of the MAPbI<sub>3</sub>-based perovskite PV cells. (c) Current density–voltage curve of the PV cell measured under 1 sun illumination. (d) Cross-section scheme of the packaged device. Light intensity-dependent (e)  $V_{out}$  and (f)  $I_{out}$  of the packaged device under periodic red LED illumination, respectively. Reprinted from Jeong *et al.*, Integrated advantages from perovskite photovoltaic cell and 2D MoTe<sub>2</sub> transistor towards self-power energy harvesting and photosensing, *Nano Energy*, **63**, 103833.<sup>135</sup> Copyright 2019, with permission from Elsevier.

photoanodes and the perovskite PSC (as power source), the system exhibited an efficient degradation of rhodamine B to almost 100% within 80 min.

## 5. Photovoltaic cells

Photovoltaic cells (PVCCs) can adjust the optical transmittance and coloration by their photovoltaic behaviors.<sup>142–144</sup> They are of interest for applications in smart windows in buildings and vehicles to manage daylight admittance. A photovoltaic device integrated with a perovskite based photovoltaic cell enables their operation without an external bias.<sup>145–147</sup> Park *et al.* used a ligand assisted re-precipitation method (LARP) to synthesize  $\text{CH}_3\text{NH}_3\text{PbX}_3$  ( $\text{X} = \text{Cl}, \text{Br}, \text{I}$ , and their mixtures) metal halide perovskite nanocrystals (MHP NCs).<sup>148</sup> The LARP method used *N,N*-dimethylformamide (DMF) as a good solvent and toluene as a poor solvent. While the good solvent possessed a slower evaporation rate, the poor solvent (toluene) induced crystallization leading to the precipitation of MHP NCs. The authors tuned the energy bandgap and corresponding absorption and emission characteristics of the MAPbX<sub>3</sub> MHP NCs by carefully adjusting the ratio of DMF and toluene. The typical size of the MAPbBr<sub>3</sub> MHP NCs was  $\sim 5$  nm. Owing to their reduced size, the MHP NCs exhibited strong luminescence and high quantum yield. The blue, green, and red MHP NCs were utilized to fabricate a panchromatic photodetector cell that showed a full-colored emission spectrum spanning 435–631 nm (Fig. 11a and b). The effective panchromatic photon harvesting was attributed to the individual absorption of blue, green, and red light by the corresponding MHP NCs and the

independent transfer of the photogenerated electrons into the mesoporous TiO<sub>2</sub> electrode. Cannavale *et al.* were amongst the first to report a self-powered photovoltaic device integrated using a perovskite and an electrochromic supercapacitor (ECS).<sup>149</sup> Here, the ECS included a layer of WO<sub>3</sub> which could store charges and change the color at the same time owing to the change of the chemical state in W. As reported, WO<sub>3</sub> is transparent, and WO<sub>3</sub><sup>+</sup> is colored.<sup>146</sup> As seen in Fig. 11c–e, once the device was exposed to solar illumination, the perovskite was capable of generating enough power to activate the coloring of WO<sub>3</sub> without requiring any external bias. Therefore, the device processed a chromic transition from semi-transparent to dark blue when irradiated by solar light. The perovskite layer presented a  $V_{oc}$  of 0.68 V, a  $J_{sc}$  of  $12.5 \text{ mA cm}^{-2}$ , an FF of 0.63, and a PCE of 5.5%. As for the PVCC, it showed average visible transmittance (AVT) of 15.9%. Illuminated at AM 1.5 sunlight, the cell's AVT changed to 5.5%. Similarly, Zhou *et al.* vertically stacked PSC with MoO<sub>3</sub>/Au/MoO<sub>3</sub> (MAM), all transparent electrode and WO<sub>3</sub> ECS to produce a photovoltaic supercapacitor (PVCCs) which can store the electrochemical energy accompanied by color change.<sup>150</sup> This design not only provided a seamless integration of energy harvesting and storage device but also improved photostability. The photocharging process changed the color of the PVCCs from transparent to dark blue. During the fully charged state, the colored PVCCs blocked off most of the light automatically turning the PSC into the low power operating state and preventing the cell from long-time exposure, thereby prolonging the device lifetime. The transparent electrodes facilitated the possibility of PSC to be illuminated from both sides. In the co-cathode structure, the FTO glass served as the co-cathode for both PSC and ECS. While for the co-anode structure, the MAM electrode served as a co-anode for



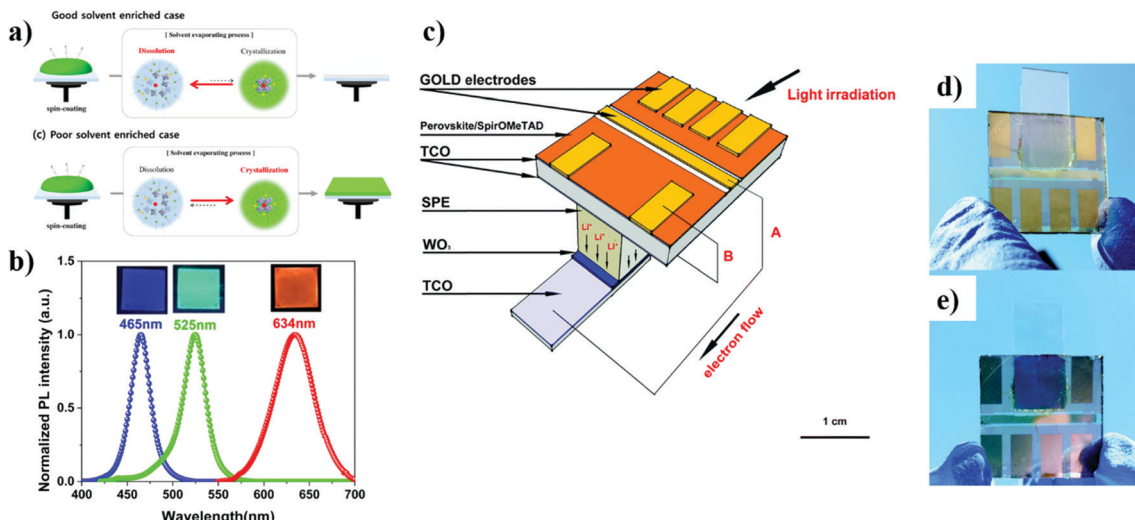


**Fig. 11** Perovskite based panchromatic photodetectors and photovoltaic devices: (a) scheme of the good–poor solvent enriched preparation process of MMH NC films by spin-coating. (b) Normalized PL spectra of blue, green, and red MHP NC-films. Reprinted from Park *et al.*, Synthesis of post-processable metal halide perovskite nanocrystals via the modified ligand-assisted re-precipitation method and their applications in self-powered panchromatic photodetectors, *J. Ind. Eng. Chem.*, **92**, 167–173.<sup>148</sup> Copyright 2020, with permission from Elsevier. (c) Scheme of axonometric view of the photovoltaic device. The optical image of the device under (d) bleached and (e) colored conditions. Reproduced from ref. 149 with permission from The Royal Society of Chemistry.

both PSC and ECS. When PSC was in the co-anode mode (or the co-cathode), PVCS with the light illumination demonstrated a  $V_{oc}$  of 0.983 V (or 1.000 V), a  $J_{sc}$  of 12.46 mA cm $^{-2}$  (or 18.17 mA cm $^{-2}$ ), an FF of 0.654% (or 0.654%), and a PCE of 8.25% (or 11.89%). With the color change, the PCEs of the co-anode and co-cathode PVCSs decreased to 3.73% and 2.26%, respectively.

## 6. Pressure sensors

Flexible pressure sensors have numerous applications in areas such as artificial electronic skins,<sup>145,151,152</sup> health monitoring devices,<sup>153–156</sup> soft robotics,<sup>157–159</sup> and wearable technology.<sup>160–165</sup> It also improves the seamless interfacing of such devices with the environment to act as a medium for information collection to drive robotics and human–artificial intelligence interactions.<sup>166</sup> The OLHP based self-powered pressure sensors and the corresponding device characteristics are listed in Table 4.

### 6.1 Mechanoluminescent device

Shohag *et al.* reported a flexible pressure sensor by integrating a mechanoluminescent device with a ~500 nm thick organometal halide perovskite.<sup>162</sup> In this work, the authors attempted at reducing the defect density of the perovskite by incorporating bromine which led to reduced trapping of charge carriers at the grain boundaries and hence, enhanced the efficiency. An applied mechanical force led the ZnS:Cu crystals to emit mechanoluminescence at ~543 nm, which could be then absorbed by the ultrathin layer of perovskite ( $\text{MAPb}(\text{Br}_{0.1}\text{I}_{0.9})_3$ ) to generate a photocurrent. The photocurrent generated in the perovskite layer increased with the increase in the intensity of light emitted from the ZnS:Cu layer, in direct proportion to the applied pressure. The sensor was able to detect pressure from 11 kPa

to 460 kPa with a sensitivity of 0.095 kPa $^{-1}$ . The sensor also exhibited a steady response over 1000 bending cycles, which is promising for monitoring health signals.

### 6.2 Piezoelectric effect assisted sensing

$\text{MAPbI}_3$  is a semi-conductor and poly(vinylidene fluoride) (PVDF) is a piezoelectric material. Researchers have combined these two materials to develop self-powered pressure sensors based on their combined properties. For example, Jella *et al.* constructed a flexible and wearable piezoelectric generator (PEG) by using the  $\text{MAPbI}_3$  perovskite and PVDF as a piezoelectric flexible polymer matrix.<sup>167</sup> The strong dipolar interactions between  $\text{MA}^+$  and the fluorine groups of the PVDF ( $-\text{CF}_2-$ ) result in a high dielectric constant, low leakage current, and high stability. As observed in Fig. 12, under an applied force, macro-dipoles are formed resulting in charge accumulation at the  $\text{MAPbI}_3$ –PVDF interface with opposite polarity, so the charge density of the electrode decreases generating a positive signal while the releasing process produced a negative signal. The device showed a  $V_{oc}$  of 45.6 V and a  $J_{sc}$  of 4.6  $\mu\text{A cm}^{-2}$  with high mechanical stability. The generated output can power commercial LEDs under a 50 N applied force by finger tapping. Sultana *et al.* produced a flexible self-powered perovskite based piezoelectric nanogenerator (P-PNG) by electrospinning PVDF nanofibers and  $\text{MAPbI}_3$ .<sup>158</sup> The mechanical vibration led to a change of output power density with a piezoelectric coefficient of ~19.7 pC N $^{-1}$  which shows appreciable potential for a pressure sensor. The  $V_{oc}$  increased with the frequency of applied stress as more charges are generated. As illustrated in Fig. 13a–d, at 4 Hz, the  $V_{oc}$  reached a maximum of 220 mV while gradually decreasing to 100 mV at 15 Hz. The authors also measured the stability of the device, which showed a stable response for 60 000 cycles at 4 Hz



Table 4 Summary of OLHP based pressure-sensitive devices and their associated parameters

Device type	Device architecture	Peak output voltage/ $V_{oc}$	Peak output current/ $J_{sc}$	Sensitivity/minimum pressure	Application and features	Ref.
Mechanoluminescent	ZnS:Cu-PDMS/PET/ITO/ SnO <sub>2</sub> /CH <sub>3</sub> NH <sub>3</sub> Pb(Br <sub>0.1</sub> I <sub>0.9</sub> ) <sub>3</sub> / Spiro-OMeTAD/Au			0.095 kPa <sup>-1</sup>	Self-powered luminescent device, 162 sensitivity range: 11 kPa to 460 kPa	162
Piezoelectric effect assisted sensor	PI-Ti/Au/PDMS/MAPbI <sub>3</sub> - PVDF/ITO-PET	45.6 V	4.7 $\mu$ A cm <sup>-2</sup>		PEG could power commercial LEDs under an applied force of 50 N, a high dielectric constant of ~56 at 1 kHz, and remanent polarization of 0.83 $\mu$ C cm <sup>-2</sup>	167
	Ni/PVDF-MAPbI <sub>3</sub> nanofiber mat/Cu	~220 mV	18.2 pA		Self-powered pyroelectric temperature sensor, pyroelectric coefficient of ~44 pC m <sup>-2</sup> K <sup>-1</sup> with a response and reset times of ~1.14 and ~1.25 s, respectively	158
	Ag/MAPbBr <sub>3</sub> -PVDF/Ag Polyester/Cu/FAPbBr <sub>2</sub> I- PVDF/Cu/polyester	~0.25 V 85 V	~30 $\mu$ A	0.02 V mm <sup>-1</sup>	Self-powered vibration sensor 168 Self-powered integrated wireless electronic node, peak output power density of 10 $\mu$ W cm <sup>-2</sup> 159	
	Glass/3 at% Al doped ZnO (AZO)/Au/AZO/MAPbI <sub>3</sub> /SiO <sub>2</sub> /AZO/Au/AZO	125.6 $\pm$ 2.4 mV and -30.2 $\pm$ 8.2 mV	0.8 nA	8.34 mV kPa <sup>-1</sup> and 0.02 nA kPa <sup>-1</sup>	Self-powered light and pressure sensor, sensitivity range: 5 to 40 kPa 169	
	ZnO nanosheets on Au/ MAPbI <sub>3</sub> /Au ITO/ZnO nanosheets on Au/ PS-MAPbI <sub>3</sub> /Au	~325 mV	~0.12 mA cm <sup>-2</sup>	0.57 kPa <sup>-1</sup>	Response speed: 0.066/0.320 s 166 Self-powered tactile sensor, sensitivity range: 0.5 kPa to 76 kPa; 170 Self-powered tactile sensor, sensitivity range: 4 Pa to 450 kPa	

with a 7.5 N applied force. Sultana *et al.* also developed a cantilever structured self-powered vibration sensor (SPVS) for low-frequency vibration detection by combining MAPbBr<sub>3</sub> and PVDF.<sup>168</sup> Based on the intrinsic properties of the PEG, the larger displacement of the tip increased the strain applied on the film resulting in an output voltage. Thus, the output voltage of the SPVS was able to sense the frequency and amplitude of vibration

with a sensitivity of 0.02 V mm<sup>-1</sup>. This device showed the possibility of detecting the vibrations from railway or construction equipment without an external bias. Recently, Khan *et al.* presented a flexible and highly porous FAPbBr<sub>2</sub>I-PVDF P-PNG assembly.<sup>159</sup> The high strain of the self-assembled highly ordered polymer scaffold and enhanced relative permittivity of the perovskite led to a 5 fold improvement in the strain-induced

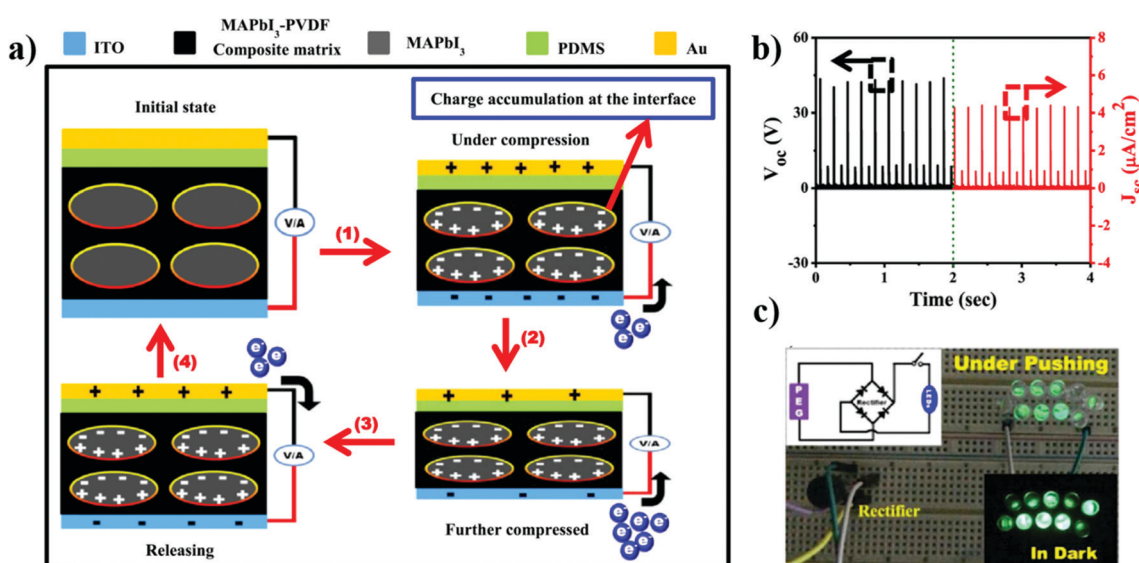


Fig. 12 Schematic of piezoelectric based origin of self-powered operation in perovskite–polymer composite and the generated response: (a) scheme of the MAPbI<sub>3</sub>–PVDF composite-based PEG working mechanism. (b) The  $V_{oc}$  and  $J_{sc}$  response of MAPbI<sub>3</sub>–PVDF PEG under an applied force of 50 N. (c) Photo images of an instant turn on 10 green LEDs by rectified electric power from the harvesting device. Insets present the scheme of the circuit and lighting of LEDs in dark. Reprinted from Jella *et al.*, Enhanced output performance of a flexible piezoelectric energy harvester based on stable MAPbI<sub>3</sub>–PVDF composite films, *Nano Energy*, **53**, 46–56.<sup>167</sup> Copyright 2018, with permission from Elsevier.



piezo potential ( $\sim 85$  V) and 15 times higher current ( $\sim 30$   $\mu$ A) in the perovskite-polymer composite P-PNG relative to those of the pristine PVDF PNG, at an applied load of 138 g. Utilizing the P-PNG, the authors further demonstrated a self-powered universal wireless electronics node (SIWEN) capable of communicating remotely with personal electronics. Energy harvesting from a real-life scenario such as automobile vibrations and biomechanical motion was also demonstrated. Eom *et al.* used the CVD method to fabricate a 500 nm thin film of  $\text{MAPbI}_3$ .<sup>169</sup> The film was stable for a month under ambient conditions. Owing to an intrinsic piezoelectric property of  $\text{MAPbI}_3$ , the device showed sensitivity to both pressure and light. The  $\text{MAPbI}_3$  film had a linear sensitivity to a pressure of  $8.34$  mV kPa $^{-1}$  and  $0.02$  nA kPa $^{-1}$  within a pressure range of 40 kPa, generated by finger touch. There was a time delay of 0.072 and 0.087 s in detection on applying and removing the pressure. The delay was attributed to the domain switching due to applied pressure on the film. In an interesting work, Saraf *et al.* combined a layer of ZnO nanosheets as a pressure-sensitive electron extraction layer on the  $\text{MAPbI}_3$  film (Fig. 13e and f).<sup>166</sup> A small external bias was applied for few minutes to the  $\text{MAPbI}_3$  film to induce polarization effects capable of generating spontaneous voltage and current response upon light illumination once the external bias was removed. The pressure applied on the top ZnO layer increased the interfacing area between the  $\text{MAPbI}_3$  film and the ZnO layer, leading to a higher collection of electrons. This action increased the value of  $J_{sc}$  (or  $V_{oc}$ ) in proportion to the

applied pressure, as shown in Fig. 13f. The sensor exhibited a linear response from 0.5 kPa to 76 kPa with a sensitivity of  $0.57$  kPa $^{-1}$ . After 100 load cycles, the device had a stable current generation density of  $0.2$  mA cm $^{-2}$ . This tactile sensor demonstrated a low energy cost as it could operate over 72 h after poling for 5 min at  $1.5$  V  $\mu$ m $^{-1}$ . To further improve the stability of the sensor, Saraf *et al.* used hydrophobic PS with  $\text{MAPbI}_3$ . The resultant polymer-perovskite hybrid device displayed stability under ambient conditions for over 1000 h.<sup>170</sup> Also, the inclusion of the polymer led to a softer film with a lower modulus which dissipated the force stimuli leading to a wide operating range. Once poled, the film was functional as a self-driven light-powered tactile sensor for 120 h and could be re-poled for continued operational performance. The light-powered tactile sensor fabricated by the assembly of 1 wt% PS- $\text{MAPbI}_3$  film and ZnO exhibited a wide operating range from 4 Pa up to 333 kPa with linear response and a sensitivity of  $19.77$  kPa $^{-1}$ .

## 7. Gas sensors

Today, there is an increasing need for portable self-powered gas sensing devices to monitor personal health, toxic gas release, and safety in public space.<sup>141,154,171–176</sup> Chen *et al.* synthesized a self-powered nitrogen dioxide (NO<sub>2</sub>) sensing device based on  $\text{FA}_{0.80}\text{MA}_{0.15}\text{Cs}_{0.05}\text{PbI}_{2.55}\text{Br}_{0.45}$  (FMCPIB) perovskites.<sup>141</sup> The authors

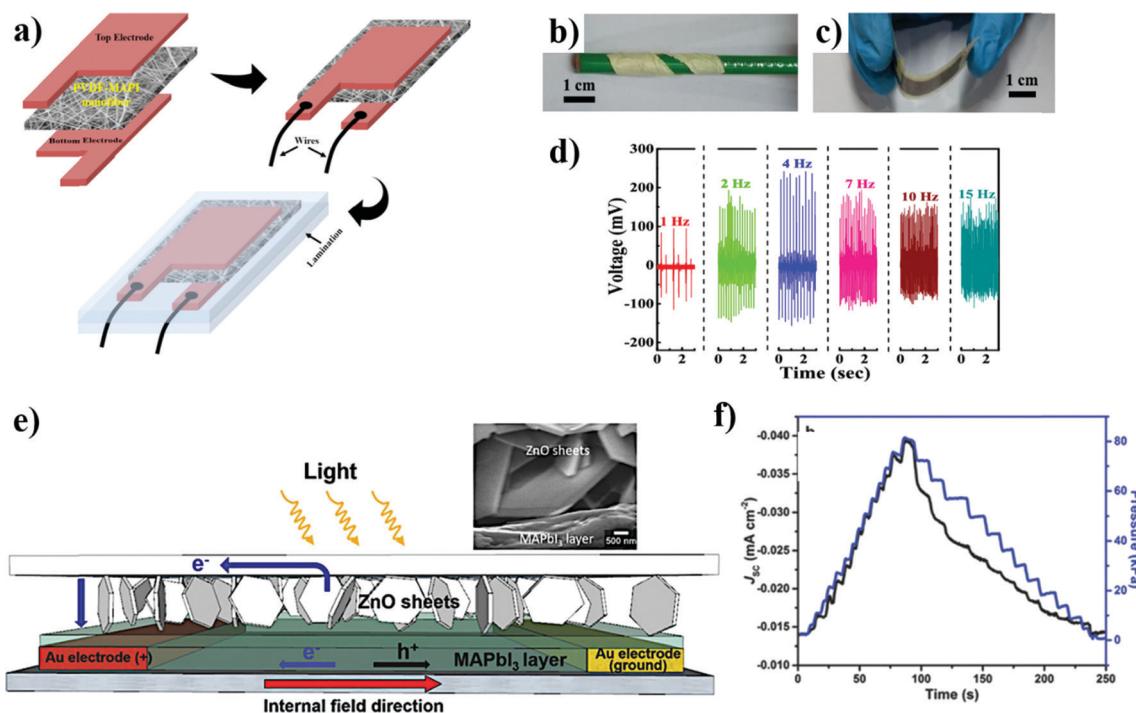


Fig. 13 Device schematic, images, and the electro-optical response of P-PNG and perovskite based self-powered tactile sensor: (a) PVDF-MAPI nanofiber mat sandwiched between two electrodes. (b) Optical image of the flexible P-PNG wrapped on a pen. (c) Optical image of bent P-PNG. (d) Output voltage response of P-PNG of applied force under different frequencies. Reprinted with permission from Sultana *et al.*, *ACS Appl. Mater. Interfaces*, **11**, 27279–27287.<sup>158</sup> Copyright © 2019 American Chemical Society. (e) Schematic of the solar-powered tactile sensor. Inset shows SEM image of ZnO sheets on the perovskite layer. (f) The response of  $J_{sc}$  under the stepped applied pressure under 1 sun illumination. Reproduced with permission from Saraf *et al.*, *Adv. Mater.*, **30**, 1705778.<sup>166</sup> © 2018 WILEY-VCH Verlag GmbH & Co. KGaA, Weinheim.



fabricated a photovoltaic cell with the vertical configuration of FTO/TiO<sub>2</sub>/FMCPIB/carbon. The authors believed that NO<sub>2</sub> can undergo interaction with the amine cation of FMCPIB. This interaction was attributed to reducing the defects in the perovskite film which decreases the charge recombination and hence increasing the density of free charge carriers. Fig. 14 represents the device performance of NO<sub>2</sub> detection at room temperature under O<sub>2</sub> rich conditions. A linear relationship up to 8 ppm with a 0.2 ppm detection limit under ambient conditions was observed. A higher NO<sub>2</sub> concentration led to a higher output current due to the interaction between NO<sub>2</sub> and FMCPIB. Owing to the functionality of the FMCPIB to act as a gas sensor, light harvester, and capacitive energy storage material (due to mobile ions), the self-powered device stayed in operation for 1.7 h in dark without requiring an external power supply. The measured response and recovery times were 17 s and 126 s, respectively. Such gas sensing ability banking on the inherent material properties of OLHP may pave new ways to monitor environmental safety using self-powered sensors.

## Challenges and future prospects

Continuous research has led to significant advances in the OLHP based self-powered devices both in terms of their performance and expanding their applications. Various devices besides solar cells, such as PDs, supercapacitors, and TENGs,

are being fabricated primarily using OLHP as a photosensitive layer. The development of self-powered electroluminescent devices using OLHP can also benefit from an increased research focus. The challenge lies in the typical high voltage requirement for generating appreciable luminescence. The use of polarization effects in OLHP is a potential route for such devices, with the research required to understand and enhance these characteristics for the generation of greater energy and electric potential. The inherent stability issue of the perovskite material is a major challenge that persists due to the inherent structure of the material (high ion mobilities) and its sensitivity to multiple external factors (such as humidity, oxygen, illumination, and temperature). Strategies such as interfacial engineering, additive integration, doping, and encapsulation are being widely adopted to reduce perovskite degradation. A significant scope also exists for the improvement of the inherent perovskite structure and composition. These combined efforts result in improving the lifetime of the OLHP based devices and should continue to progress them towards commercial viability. With the concerns of toxicity surrounding lead, there are ongoing efforts of substituting it with other divalent ions such as Sn, Ge, Bi, and Sb, but the resulting reduction in performance needs to be addressed in order to develop lead-free perovskites.<sup>177,178</sup>

At a macroscale, as it stands, the majority of OLHP based self-powered devices and sensors are rigid. Although, in the last

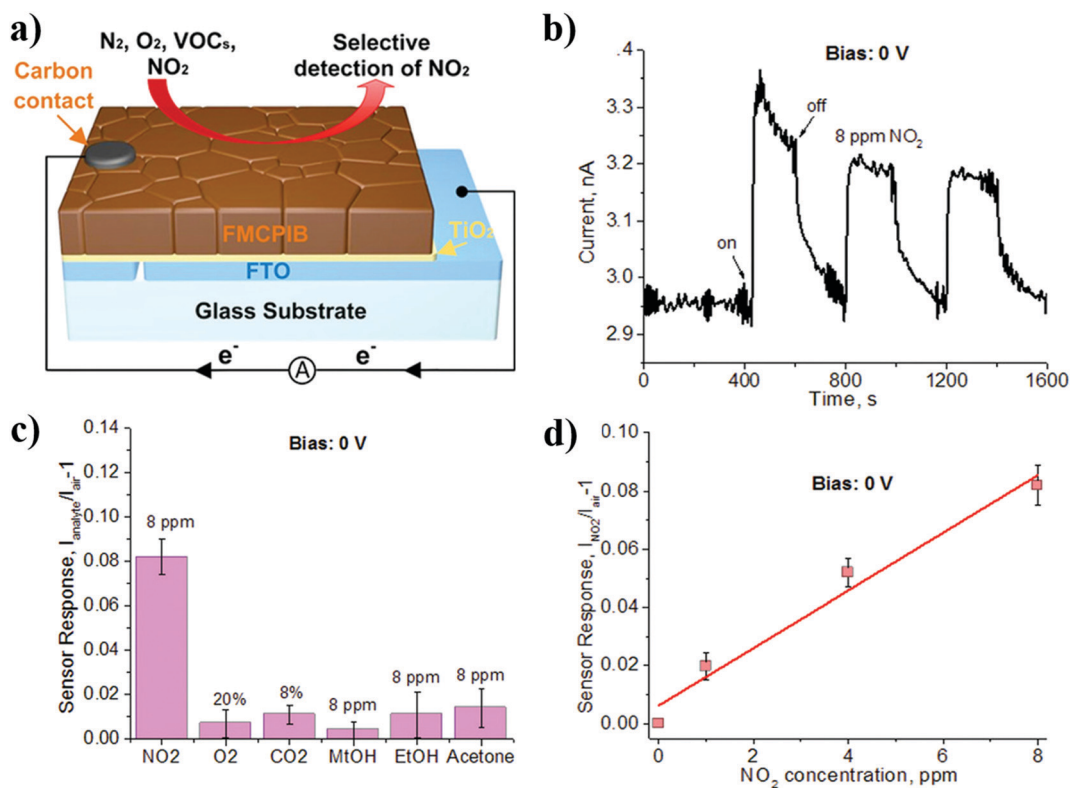


Fig. 14 Design and self-powered chemical response of the FMCPIB-based gas sensor at room temperature: (a) scheme of the FMCPIB-based gas sensor. (b) The current response of the FMCPIB devices with the injection of 8 ppm NO<sub>2</sub>. (c) The sensor response for six different gases. (d) The sensor response as a function of the NO<sub>2</sub> concentration in the self-powered mode. Reproduced with permission from Chen *et al.*, *Adv. Opt. Mater.*, **8**, 1901863.<sup>141</sup> © 2020 WILEY-VCH Verlag GmbH & Co. KGaA, Weinheim.



few years flexible transducers are being researched and reported with greater intensity, they experience performance degradation during long-term operations. Most wearable and portable electronic devices and sensors mandate the ability to be stretched and bent over a couple of thousand cycles without incurring significant decay in output over time. Alternatives for 3D OLHP such as 2D, 1D, and 0D OLHP may offer enhanced flexibility and might provide viable options.<sup>179–182</sup> Equally critical is the need for developing appropriate substrates and electrodes for long-term device operation while ensuring wearability comfort. Furthermore, it is worth considering that almost all OLHP self-powered portable and wearable devices are tested at 1 sun. However, the indoor performance of these devices with limited illumination is rarely reported. Therefore, developing standard protocols for testing devices under such limited light conditions need to be developed as this will allow a more accurate comparison of devices.

Although low levels of the output signals and non-continuous operation seem to impede the overall capability of the OLHP based self-driven devices and sensors, several other major factors contribute to hinder the commercial viability of such perovskite-based transducers. Currently, there is a lack of a standardized large-scale manufacturing process that could ensure performance consistency amongst batches of the same device. Besides, there is limited research available over performance–cost analysis specific to the OLHP self-powered devices that could drive them from a lab prototype to a commercial finished product. OLHP is considered a low-cost material compared to other semiconductors (such as Si and organic compounds); however, a more detailed cost analysis is required for the quantification of its cost advantage (including Pb recycling needs). Techniques such as printing need to be promoted to drive up large scale cost-effective production of the OLHP based self-powered devices. The use of advanced micro-fabrication and nanofabrication techniques can further expand the integration of other flexible electronic, photonic, and optoelectronic devices with OLHP as an energy harvester.

In summary, significant advancements have been made in OLHP based self-powered applications, but still there are critical challenges that need to be addressed before they can be considered commercially viable products. The rapid development of materials science, processing, and manufacturing technology can enable the progress of the OLHP based self-powered system in our day-to-day life at a rapid pace and the commercialization of OLHP based photovoltaic cells provides important lessons for this road map.

## Author contributions

Avi Mathur: conceptualization, investigation, and writing – original draft. Hua Fan: investigation and writing – original draft. Vivek Maheshwari: conceptualization, funding acquisition, resources, writing – review & editing, and supervision.

## Conflicts of interest

There are no conflicts to declare.

## Acknowledgements

This work was supported by the University of Waterloo, Gerald Schwartz and Heather Reisman Foundation, Canada Foundation for Innovation, Early Researcher Award from the Ministry of Research and Innovation and Science, Ontario, and NSERC Canada.

## References

- 1 L. Atzori, A. Iera and G. Morabito, *Comput. Networks*, 2010, **54**, 2787–2805.
- 2 F. Xia, L. T. Yang, L. Wang and A. Vinel, *Int. J. Commun. Syst.*, 2012, **25**, 1101.
- 3 Y. Yuehong, Y. Zeng, X. Chen and Y. Fan, *J. Ind. Inf. Integr.*, 2016, **1**, 3–13.
- 4 C. Xu, Y. Song, M. Han and H. Zhang, *Microsyst. Nanoeng.*, 2021, **7**, 1–14.
- 5 M. J. Cima, *Nat. Biotechnol.*, 2014, **32**, 642–643.
- 6 N. Xu, S. Rangwala, K. K. Chintalapudi, D. Ganesan, A. Broad, R. Govindan and D. Estrin, *A wireless sensor network for structural monitoring*, 2004.
- 7 J. Kim, R. A. Swartz, J. P. Lynch, J.-J. Lee and C.-G. Lee, *Smart Struct. Syst.*, 2010, **6**, 505–524.
- 8 F. Zhang, X. Liu, S. A. Hackworth, R. J. Sclabassi and M. Sun, *In vitro* and *in vivo* studies on wireless powering of medical sensors and implantable devices, IEEE, 2009.
- 9 D. Fitzpatrick, *Implantable electronic medical devices*, Elsevier, 2014.
- 10 F. Larsson, P. Andersson, P. Blomqvist and B.-E. Mellander, *Sci. Rep.*, 2017, **7**, 1–13.
- 11 J. Sun, J. Li, T. Zhou, K. Yang, S. Wei, N. Tang, N. Dang, H. Li, X. Qiu and L. Chen, *Nano Energy*, 2016, **27**, 313–319.
- 12 R. W. Keyes, *IBM J. Res. Dev.*, 1988, **32**, 84–88.
- 13 P. Glynne-Jones and N. White, *Sens. Rev.*, 2001, **21**, 91–98.
- 14 Q. Zheng, Q. Tang, Z. L. Wang and Z. Li, *Nat. Rev. Cardiol.*, 2020, 1–15.
- 15 K. M. Reilly, M. T. Birner and N. G. Johnson, Measuring air quality using wireless self-powered devices, IEEE, 2015.
- 16 Z. Liu, B. Cho, T. Ouyang and B. Feldman, *Anal. Chem.*, 2012, **84**, 3403–3409.
- 17 F.-R. Fan, L. Lin, G. Zhu, W. Wu, R. Zhang and Z. L. Wang, *Nano Lett.*, 2012, **12**, 3109–3114.
- 18 J. Zhao, R. Ghannam, K. O. Htet, Y. Liu, M. K. Law, V. A. Roy, B. Michel, M. A. Imran and H. Heidari, *Adv. Healthcare Mater.*, 2020, **9**, 2000779.
- 19 J. Twidell and T. Weir, *Renewable energy resources*, Routledge, 2015.
- 20 A. Kojima, K. Teshima, Y. Shirai and T. Miyasaka, *J. Am. Chem. Soc.*, 2009, **131**, 6050–6051.
- 21 National Renewable Energy Laboratory – Best research-cell efficiencies chart, <https://www.nrel.gov/pv/cell-efficiency.html>, accessed April, 2021.
- 22 K. P. Ong, T. W. Goh, Q. Xu and A. Huan, *J. Phys. Chem. A*, 2015, **119**, 11033–11038.



23 C. Quarti, E. Mosconi, J. M. Ball, V. D'Innocenzo, C. Tao, S. Pathak, H. J. Snaith, A. Petrozza and F. De Angelis, *Energy Environ. Sci.*, 2016, **9**, 155–163.

24 Q. Chen, N. De Marco, Y. M. Yang, T.-B. Song, C.-C. Chen, H. Zhao, Z. Hong, H. Zhou and Y. Yang, *Nano Today*, 2015, **10**, 355–396.

25 F. Hao, C. C. Stoumpos, D. H. Cao, R. P. Chang and M. G. Kanatzidis, *Nat. Photonics*, 2014, **8**, 489.

26 L. Chouhan, S. Ghimire, C. Subrahmanyam, T. Miyasaka and V. Biju, *Chem. Soc. Rev.*, 2020, **49**, 2869–2885.

27 S. Pang, H. Hu, J. Zhang, S. Lv, Y. Yu, F. Wei, T. Qin, H. Xu, Z. Liu and G. Cui, *Chem. Mater.*, 2014, **26**, 1485–1491.

28 J. Song, J. Li, X. Li, L. Xu, Y. Dong and H. Zeng, *Adv. Mater.*, 2015, **27**, 7162–7167.

29 Q. Shan, J. Song, Y. Zou, J. Li, L. Xu, J. Xue, Y. Dong, B. Han, J. Chen and H. Zeng, *Small*, 2017, **13**, 1701770.

30 L. Xu, J. Li, B. Cai, J. Song, F. Zhang, T. Fang and H. Zeng, *Nat. Commun.*, 2020, **11**, 1–12.

31 J. Chen, J. Wang, X. Xu, J. Li, J. Song, S. Lan, S. Liu, B. Cai, B. Han and J. T. Precht, *Nat. Photonics*, 2021, **15**, 238–244.

32 J. Sun, J. Wu, X. Tong, F. Lin, Y. Wang and Z. M. Wang, *Adv. Sci.*, 2018, **5**, 1700780.

33 R. Saraf and V. Maheshwari, *Functional Tactile Sensors*, Elsevier, 2021, pp. 141–158.

34 X. Zhang, X. Dong, S. Wang, H. Liu, W. Hu and X. Li, *Chem. Eng. J.*, 2021, **404**, 125957.

35 F. P. G. de Arquer, A. Armin, P. Meredith and E. H. Sargent, *Nat. Rev. Mater.*, 2017, **2**, 1–17.

36 Y. Xie, B. Zhang, S. Wang, D. Wang, A. Wang, Z. Wang, H. Yu, H. Zhang, Y. Chen and M. Zhao, *Adv. Mater.*, 2017, **29**, 1605972.

37 E. Dupont, M. Byloos, M. Gao, M. Buchanan, C.-Y. Song, Z. Wasilewski and H. Liu, *IEEE Photonics Technol. Lett.*, 2002, **14**, 182–184.

38 C. Chen, K. Choi, W. Chang and D. Tsui, *Appl. Phys. Lett.*, 1998, **72**, 7–9.

39 S. Donati, *Photodetectors: devices, circuits and applications*, John Wiley & Sons, 2021.

40 G. Konstantatos, *Nat. Commun.*, 2018, **9**, 5266.

41 X. Feng, M. Tan, M. Li, H. Wei and B. Yang, *Nano Lett.*, 2021, **21**, 1500–1507.

42 Y. Liu, Y. Zhang, X. Zhu, Z. Yang, W. Ke, J. Feng, X. Ren, K. Zhao, M. Liu and M. G. Kanatzidis, *Sci. Adv.*, 2021, **7**, eabc8844.

43 T. M. H. Nguyen, S. Kim and C. W. Bark, *J. Mater. Chem. A*, 2021, **9**, 1269–1276.

44 C. Perumal Veeramalai, S. Feng, X. Zhang, S. V. N. Pammi, V. Pecunia and C. Li, *Photonics Res.*, 2021, **9**, 968–991.

45 L. Dou, Y. M. Yang, J. You, Z. Hong, W.-H. Chang, G. Li and Y. Yang, *Nat. Commun.*, 2014, **5**, 1–6.

46 M. Zhang, M. Ye, W. Wang, C. Ma, S. Wang, Q. Liu, T. Lian, J. Huang and Z. Lin, *Adv. Mater.*, 2020, **32**, 2000999.

47 B. Wang, M. Zhang, X. Cui, Z. Wang, M. Rager, Y. Yang, Z. Zou, Z. L. Wang and Z. Lin, *Angew. Chem.*, 2020, **132**, 1628–1635.

48 M. Zhang, X. Cui, Y. Wang, B. Wang, M. Ye, W. Wang, C. Ma and Z. Lin, *Nano Energy*, 2020, **71**, 104620.

49 Z. Wang, R. Yu, C. Pan, Z. Li, J. Yang, F. Yi and Z. L. Wang, *Nat. Commun.*, 2015, **6**, 1–7.

50 J. Yu, X. Chen, Y. Wang, H. Zhou, M. Xue, Y. Xu, Z. Li, C. Ye, J. Zhang and P. A. Van Aken, *J. Mater. Chem. C*, 2016, **4**, 7302–7308.

51 Y. Zhu, Z. Song, H. Zhou, D. Wu, R. Lu, R. Wang and H. Wang, *Appl. Surf. Sci.*, 2018, **448**, 23–29.

52 H. Zhou, L. Yang, P. Gui, C. R. Grice, Z. Song, H. Wang and G. Fang, *Sol. Energy Mater. Sol. Cells*, 2019, **193**, 246–252.

53 X. Yang, Y. Zhu, H. Zhou, Z. Song, R. Liu, L. Shen and H. Wang, *Appl. Surf. Sci.*, 2020, **504**, 144468.

54 Z. Liu, X. Liu, B. Sun, X. Tan, H. Ye, J. Zhou, Z. Tang, T. Shi and G. Liao, *Adv. Mater. Technol.*, 2020, **5**, 2000260.

55 H. Zhou, J. Mei, M. Xue, Z. Song and H. Wang, *J. Phys. Chem. C*, 2017, **121**, 21541–21545.

56 J. Ghosh, G. Natu and P. Giri, *Org. Electron.*, 2019, **71**, 175–184.

57 D. H. Shin, S. H. Shin, S. G. Lee, S. Kim and S.-H. Choi, *ACS Sustainable Chem. Eng.*, 2019, **7**, 19961–19968.

58 Y. Cheng, Z. Shi, S. Yin, Y. Li, S. Li, W. Liang, D. Wu, Y. Tian and X. Li, *Sol. Energy Mater. Sol. Cells*, 2020, **204**, 110230.

59 L. Shen, Y. Fang, D. Wang, Y. Bai, Y. Deng, M. Wang, Y. Lu and J. Huang, *Adv. Mater.*, 2016, **28**, 10794–10800.

60 Q. Shan, C. Wei, Y. Jiang, J. Song, Y. Zou, L. Xu, T. Fang, T. Wang, Y. Dong and J. Liu, *Light: Sci. Appl.*, 2020, **9**, 1–9.

61 C. Lan, H. Zou, L. Wang, M. Zhang, S. Pan, Y. Ma, Y. Qiu, Z. L. Wang and Z. Lin, *Adv. Mater.*, 2020, **32**, 2005481.

62 Z. Li, H. Li, K. Jiang, D. Ding, J. Li, C. Ma, S. Jiang, Y. Wang, T. D. Anthopoulos and Y. Shi, *ACS Appl. Mater. Interfaces*, 2019, **11**, 40204–40213.

63 T. Pang, R. Jia, Y. Wang, K. Sun, Z. Hu, Y. Zhu, S. Luan and Y. Zhang, *J. Mater. Chem. C*, 2019, **7**, 609–616.

64 L. Ren, M. Wang, M. Li, S. Wang, S. Wang, Y. Zhao, M. A. Iqbal and K. Jin, *Opt. Mater.*, 2020, **100**, 109687.

65 K. Pandey, M. Chauhan, V. Bhatt, B. Tripathi, P. Yadav and M. Kumar, *RSC Adv.*, 2016, **6**, 105076–105080.

66 J. Li, S. Yuan, G. Tang, G. Li, D. Liu, J. Li, X. Hu, Y. Liu, J. Li and Z. Yang, *ACS Appl. Mater. Interfaces*, 2017, **9**, 42779–42787.

67 Q. Zeng and Z. Liu, *Adv. Electron. Mater.*, 2018, **4**, 1700335.

68 M. Pandey, R. Soni, A. Mathur, A. Singh, A. K. Singh, S. Raghavan and U. Chandni, *Phys. Rev. Appl.*, 2019, **12**, 064032.

69 D. Sarkar, W. Liu, X. Xie, A. C. Anselmo, S. Mitragotri and K. Banerjee, *ACS Nano*, 2014, **8**, 3992–4003.

70 N. Rohaizad, C. C. Mayorga-Martinez, Z. K. Sofer and M. Pumera, *ACS Appl. Mater. Interfaces*, 2017, **9**, 40697–40706.

71 S. Barua, H. S. Dutta, S. Gogoi, R. Devi and R. Khan, *ACS Appl. Nano Mater.*, 2017, **1**, 2–25.

72 J. H. Lee, J. Y. Park, E. B. Cho, T. Y. Kim, S. A. Han, T. H. Kim, Y. Liu, S. K. Kim, C. J. Roh and H. J. Yoon, *Adv. Mater.*, 2017, **29**, 1606667.

73 A. Di Bartolomeo, A. Grillo, F. Urban, L. Iemmo, F. Giubileo, G. Luongo, G. Amato, L. Croin, L. Sun and S. J. Liang, *Adv. Funct. Mater.*, 2018, **28**, 1800657.



74 F. Bai, J. Qi, F. Li, Y. Fang, W. Han, H. Wu and Y. Zhang, *Adv. Mater. Interfaces*, 2018, **5**, 1701275.

75 L. H. Zeng, Q. M. Chen, Z. X. Zhang, D. Wu, H. Yuan, Y. Y. Li, W. Qarony, S. P. Lau, L. B. Luo and Y. H. Tsang, *Adv. Sci.*, 2019, **6**, 1901134.

76 Y. Kutes, L. Ye, Y. Zhou, S. Pang, B. D. Huey and N. P. Padture, *J. Phys. Chem. Lett.*, 2014, **5**, 3335–3339.

77 J. M. Frost, K. T. Butler, F. Brivio, C. H. Hendon, M. Van Schilfgaarde and A. Walsh, *Nano Lett.*, 2014, **14**, 2584–2590.

78 L. M. Garten, D. T. Moore, S. U. Nanayakkara, S. Dwaraknath, P. Schulz, J. Wands, A. Rockett, B. Newell, K. A. Persson and S. Trolier-McKinstry, *Sci. Adv.*, 2019, **5**, eaas9311.

79 A. Gómez, Q. Wang, A. R. Goñi, M. Campoy-Quiles and A. Abate, *Energy Environ. Sci.*, 2019, **12**, 2537–2547.

80 Z. Fan, J. Xiao, K. Sun, L. Chen, Y. Hu, J. Ouyang, K. P. Ong, K. Zeng and J. Wang, *J. Phys. Chem. Lett.*, 2015, **6**, 1155–1161.

81 M. N. F. Hoque, M. Yang, Z. Li, N. Islam, X. Pan, K. Zhu and Z. Fan, *ACS Energy Lett.*, 2016, **1**, 142–149.

82 R. Saraf and V. Maheshwari, *ACS Appl. Mater. Interfaces*, 2018, **10**, 21066–21072.

83 A. Mathur, A. Li and V. Maheshwari, *J. Phys. Chem. Lett.*, 2021, **12**, 1481–1489.

84 F. Cao, W. Tian, M. Wang and L. Li, *ACS Photonics*, 2018, **5**, 3731–3738.

85 F. Cao, W. Tian, L. Meng, M. Wang and L. Li, *Adv. Funct. Mater.*, 2019, **29**, 1808415.

86 F. Cao, W. Tian, M. Wang, H. Cao and L. Li, *Adv. Funct. Mater.*, 2019, **29**, 1901280.

87 L. Su, Z. X. Zhao, H. Y. Li, J. Yuan, Z. L. Wang, G. Z. Cao and G. Zhu, *ACS Nano*, 2015, **9**, 11310–11316.

88 V. K. Hsiao, S.-F. Leung, Y.-C. Hsiao, P.-K. Kung, Y.-C. Lai, Z.-H. Lin, K. N. Salama, H. N. Alshareef, Z. L. Wang and J.-H. He, *Nano Energy*, 2019, **65**, 103958.

89 H. Guo, J. Zhao, Q. Dong, L. Wang, X. Ren, S. Liu, C. Zhang and G. Dong, *Nano Energy*, 2019, **56**, 391–399.

90 S. F. Leung, K. T. Ho, P. K. Kung, V. K. Hsiao, H. N. Alshareef, Z. L. Wang and J. H. He, *Adv. Mater.*, 2018, **30**, 1704611.

91 R. Saraf, A. Mathur and V. Maheshwari, *ACS Appl. Mater. Interfaces*, 2020, **12**, 25011–25019.

92 H. Fang, Q. Li, J. Ding, N. Li, H. Tian, L. Zhang, T. Ren, J. Dai, L. Wang and Q. Yan, *J. Mater. Chem. C*, 2016, **4**, 630–636.

93 J. Ding, H. Fang, Z. Lian, J. Li, Q. Lv, L. Wang, J.-L. Sun and Q. Yan, *CrystEngComm*, 2016, **18**, 4405–4411.

94 M. Cao, J. Tian, Z. Cai, L. Peng, L. Yang and D. Wei, *Appl. Phys. Lett.*, 2016, **109**, 233303.

95 X. Pan, H. Zhou, R. Liu, D. Wu, Z. Song, X. Tang, X. Yang and H. Wang, *J. Mater. Chem. C*, 2020, **8**, 2028–2035.

96 C. Perumal Veeramalai, S. Yang, R. Zhi, M. Sulaman, M. I. Saleem, Y. Cui, Y. Tang, Y. Jiang, L. Tang and B. Zou, *Adv. Opt. Mater.*, 2020, **8**, 2000215.

97 G. Tong, X. Geng, Y. Yu, L. Yu, J. Xu, Y. Jiang, Y. Sheng, Y. Shi and K. Chen, *RSC Adv.*, 2017, **7**, 18224–18230.

98 G. R. Adams, V. O. Eze, L. B. Carani, A. Pino, C. Jolowsky and O. I. Okoli, *RSC Adv.*, 2020, **10**, 18139–18146.

99 S. Pammi, R. Maddaka, V.-D. Tran, J.-H. Eom, V. Pecunia, S. Majumder, M.-D. Kim and S. G. Yoon, *Nano Energy*, 2020, **74**, 104872.

100 S. V. N. Pammi, V. D. Tran, R. Maddaka, J. H. Eom, J. S. Jung, H. M. Jeong, M. D. Kim, V. Pecunia and S. G. Yoon, *Adv. Opt. Mater.*, 2020, **8**, 2000845.

101 S. Sadhasivam, A. Gunasekaran, N. Anbarasan, M. Mukilan and K. Jeganathan, *Mater. Lett.*, 2020, **276**, 128155.

102 J. Wang, S. Xiao, W. Qian, K. Zhang, J. Yu, X. Xu, G. Wang, S. Zheng and S. Yang, *Adv. Mater.*, 2021, **33**, 2005557.

103 W. Wang, D. Zhao, F. Zhang, L. Li, M. Du, C. Wang, Y. Yu, Q. Huang, M. Zhang and L. Li, *Adv. Funct. Mater.*, 2017, **27**, 1703953.

104 H. L. Zhu, H. Lin, Z. Song, Z. Wang, F. Ye, H. Zhang, W.-J. Yin, Y. Yan and W. C. Choy, *ACS Nano*, 2019, **13**, 11800–11808.

105 H. Sun, W. Tian, X. Wang, K. Deng, J. Xiong and L. Li, *Adv. Mater.*, 2020, **32**, 1908108.

106 F. Cao, Q. Liao, K. Deng, L. Chen, L. Li and Y. Zhang, *Nano Res.*, 2018, **11**, 1722–1730.

107 C. Bao, W. Zhu, J. Yang, F. Li, S. Gu, Y. Wang, T. Yu, J. Zhu, Y. Zhou and Z. Zou, *ACS Appl. Mater. Interfaces*, 2016, **8**, 23868–23875.

108 H. Sun, T. Lei, W. Tian, F. Cao, J. Xiong and L. Li, *Small*, 2017, **13**, 1701042.

109 H. Sun, W. Tian, F. Cao, J. Xiong and L. Li, *Adv. Mater.*, 2018, **30**, 1706986.

110 G. R. Adams, N. Adhikari, H. Parker and O. Okoli, *Adv. Mater. Interfaces*, 2018, **5**, 1800082.

111 S. Lim, M. Ha, Y. Lee and H. Ko, *Adv. Opt. Mater.*, 2018, **6**, 1800615.

112 M. Wang, F. Cao, L. Meng, W. Tian and L. Li, *Adv. Mater. Interfaces*, 2019, **6**, 1801526.

113 W. Tian, L. Min, F. Cao and L. Li, *Adv. Mater.*, 2020, **32**, 1906974.

114 D. H. Shin, J. S. Ko, S. K. Kang and S.-H. Choi, *ACS Appl. Mater. Interfaces*, 2020, **12**, 4586–4593.

115 D. H. Shin, S. H. Shin and S.-H. Choi, *Appl. Surf. Sci.*, 2020, **514**, 145880.

116 J. Tao, Z. Xiao, J. Wang, C. Li, X. Sun, F. Li, X. Zou, G. Liao and Z. Zou, *J. Alloys Compd.*, 2020, **845**, 155311.

117 R. Saraf, H. Fan and V. Maheshwari, *npj Flexible Electron.*, 2020, **4**, 1–8.

118 A. Gurung, K. M. Reza, S. Mabrouk, B. Bahrami, R. Pathak, B. S. Lamsal, S. I. Rahman, N. Ghimire, R. S. Bobba, K. Chen, J. Pokharel, A. Baniya, M. A. R. Laskar, M. Liang, W. Zhang, W.-H. Zhang, S. Yang, K. Xu and Q. Qiao, *Adv. Funct. Mater.*, 2020, **30**, 2001865.

119 A. Das, S. Deshagani, R. Kumar and M. Deepa, *ACS Appl. Mater. Interfaces*, 2018, **10**, 35932–35945.

120 S. Yun, Y. Zhang, Q. Xu, J. Liu and Y. Qin, *Nano Energy*, 2019, **60**, 600–619.

121 J. Xu, Y. Chen and L. Dai, *Nat. Commun.*, 2015, **6**, 8103.

122 S. J. Varma, K. S. Kumar, S. Seal, S. Rajaraman and J. Thomas, *Adv. Sci.*, 2018, **5**, 1800340.

123 S. Yun, Y. Qin, A. R. Uhl, N. Vlachopoulos, M. Yin, D. Li, X. Han and A. Hagfeldt, *Energy Environ. Sci.*, 2018, **11**, 476–526.



124 P. Dong, M.-T. F. Rodrigues, J. Zhang, R. S. Borges, K. Kalaga, A. L. M. Reddy, G. G. Silva, P. M. Ajayan and J. Lou, *Nano Energy*, 2017, **42**, 181–186.

125 B. Luo, D. Ye and L. Wang, *Adv. Sci.*, 2017, **4**, 1700104.

126 H. Meng, S. Pang and G. Cui, *ChemSusChem*, 2019, **12**, 3431–3447.

127 C. Li, S. Cong, Z. Tian, Y. Song, L. Yu, C. Lu, Y. Shao, J. Li, G. Zou, M. H. Rümmeli, S. Dou, J. Sun and Z. Liu, *Nano Energy*, 2019, **60**, 247–256.

128 P. Du, X. Hu, C. Yi, H. C. Liu, P. Liu, H.-L. Zhang and X. Gong, *Adv. Funct. Mater.*, 2015, **25**, 2420–2427.

129 R. Liu, C. Liu and S. Fan, *J. Mater. Chem. A*, 2017, **5**, 23078–23084.

130 C. Boyer and S. Roy, *IEEE Trans. Commun.*, 2014, **62**, 770–785.

131 S. N. R. Kantareddy, I. Mathews, S. Sun, M. Layurova, J. Thapa, J. Correa-Baena, R. Bhattacharyya, T. Buonassisi, S. E. Sarma and I. M. Peters, *IEEE Sens. J.*, 2020, **20**, 471–478.

132 I. Mathews, S. N. R. Kantareddy, S. Sun, M. Layurova, J. Thapa, J.-P. Correa-Baena, R. Bhattacharyya, T. Buonassisi, S. Sarma and I. M. Peters, *Adv. Funct. Mater.*, 2019, **29**, 1904072.

133 M. Li, F. Igbari, Z.-K. Wang and L.-S. Liao, *Adv. Energy Mater.*, 2020, **10**, 2000641.

134 K. Wojciechowski, D. Forgács and T. Rivera, *Sol. RRL*, 2019, **3**, 1900144.

135 Y. Jeong, D. Shin, J. H. Park, J. Park, Y. Yi and S. Im, *Nano Energy*, 2019, **63**, 103833.

136 W. Yu, F. Li, L. Yu, M. R. Niazi, Y. Zou, D. Corzo, A. Basu, C. Ma, S. Dey, M. L. Tietze, U. Buttner, X. Wang, Z. Wang, M. N. Hedhili, C. Guo, T. Wu and A. Amassian, *Nat. Commun.*, 2018, **9**, 5354.

137 V. Q. Dang, G.-S. Han, T. Q. Trung, L. T. Duy, Y.-U. Jin, B.-U. Hwang, H.-S. Jung and N.-E. Lee, *Carbon*, 2016, **105**, 353–361.

138 S.-h. Lee, J. Y. Kim, S. Choi, Y. Lee, K.-S. Lee, J. Kim and J. Joo, *ACS Appl. Mater. Interfaces*, 2020, **12**, 25159–25167.

139 Y. Chen, X. Wu, Y. Chu, J. Zhou, B. Zhou and J. Huang, *Nano-Micro Lett.*, 2018, **10**, 57.

140 D. Chen, Y. Lu, J. Wu, N. Li, Y.-Z. Zheng and X. Tao, *J. Phys. Chem. Solids*, 2019, **132**, 204–212.

141 H. Chen, M. Zhang, B. Xing, X. Fu, R. Bo, H. K. Mulmudi, S. Huang, A. W. Y. Ho-Baillie, K. R. Catchpole and A. Tricoli, *Adv. Opt. Mater.*, 2020, **8**, 1901863.

142 M. Pugliese, F. Bisconti, A. Rizzo, S. Colella, C. T. Prontera, G. Gigli, V. Maiorano and P. Cossari, *ACS Appl. Energy Mater.*, 2020, **3**, 10453–10462.

143 F. Favoino, F. Fiorito, A. Cannavale, G. Ranzi and M. Overend, *Appl. Energy*, 2016, **178**, 943–961.

144 F. Malara, A. Cannavale, S. Carallo and G. Gigli, *ACS Appl. Mater. Interfaces*, 2014, **6**, 9290–9297.

145 Z. Xu, C. Wu, Y. Zhu, S. Ju, F. Ma, T. Guo, F. Li and T. Whan Kim, *Nanoscale*, 2021, **13**, 253–260.

146 C. Bechinger, S. Ferrere, A. Zaban, J. Sprague and B. A. Gregg, *Nature*, 1996, **383**, 608–610.

147 N. C. Davy, M. Sezen-Edmonds, J. Gao, X. Lin, A. Liu, N. Yao, A. Kahn and Y.-L. Loo, *Nat. Energy*, 2017, **2**, 1–11.

148 J. K. Park, J. H. Heo, B. W. Kim and S. H. Im, *J. Ind. Eng. Chem.*, 2020, **92**, 167–173.

149 A. Cannavale, G. E. Eperon, P. Cossari, A. Abate, H. J. Snaith and G. Gigli, *Energy Environ. Sci.*, 2015, **8**, 1578–1584.

150 F. Zhou, Z. Ren, Y. Zhao, X. Shen, A. Wang, Y. Y. Li, C. Surya and Y. Chai, *ACS Nano*, 2016, **10**, 5900–5908.

151 Y. Ai, Z. Lou, S. Chen, D. Chen, Z. M. Wang, K. Jiang and G. Shen, *Nano Energy*, 2017, **35**, 121–127.

152 L. Gu, M. M. Tavakoli, D. Zhang, Q. Zhang, A. Waleed, Y. Xiao, K.-H. Tsui, Y. Lin, L. Liao, J. Wang and Z. Fan, *Adv. Mater.*, 2016, **28**, 9713–9721.

153 D. Y. Park, D. J. Joe, D. H. Kim, H. Park, J. H. Han, C. K. Jeong, H. Park, J. G. Park, B. Joung and K. J. Lee, *Adv. Mater.*, 2017, **29**, 1702308.

154 D. B. Kim, K. H. Park and Y. S. Cho, *Energy Environ. Sci.*, 2020, **13**, 2077–2086.

155 F. Mokhtari, Z. Cheng, R. Raad, J. Xi and J. Foroughi, *J. Mater. Chem. A*, 2020, **8**, 9496–9522.

156 Z. Wu, J. Yang, X. Sun, Y. Wu, L. Wang, G. Meng, D. Kuang, X. Guo, W. Qu, B. Du, C. Liang, X. Fang, X. Tang and Y. He, *Sens. Actuators, B*, 2021, **337**, 129772.

157 S. Ippili, V. Jella, S. Eom, S. Hong and S.-G. Yoon, *ACS Appl. Mater. Interfaces*, 2020, **12**, 50472–50483.

158 A. Sultana, S. K. Ghosh, M. M. Alam, P. Sadhukhan, K. Roy, M. Xie, C. R. Bowen, S. Sarkar, S. Das, T. R. Middya and D. Mandal, *ACS Appl. Mater. Interfaces*, 2019, **11**, 27279–27287.

159 A. A. Khan, M. M. Rana, G. Huang, N. Mei, R. Saritas, B. Wen, S. Zhang, P. Voss, E.-A. Rahman, Z. Leonenko, S. Islam and D. Ban, *J. Mater. Chem. A*, 2020, **8**, 13619–13629.

160 S. Ippili, V. Jella, J. Kim, S. Hong and S.-G. Yoon, *Nano Energy*, 2018, **49**, 247–256.

161 Z. Zhao, Y. Dai, S. X. Dou and J. Liang, *Mater. Today Energy*, 2021, **20**, 100690.

162 M. A. S. Shohag, V. O. Eze, L. Braga Carani and O. I. Okoli, *ACS Appl. Nano Mater.*, 2020, **3**, 6749–6756.

163 Z. Gu, Z. Huang, X. Hu, Y. Wang, L. Li, M. Li and Y. Song, *ACS Appl. Mater. Interfaces*, 2020, **12**, 22157–22162.

164 J. Choi, D. Kwon, B. Kim, K. Kang, J. Gu, J. Jo, K. Na, J. Ahn, D. Del Orbe and K. Kim, *Nano Energy*, 2020, **74**, 104749.

165 F. He, X. You, H. Gong, Y. Yang, T. Bai, W. Wang, W. Guo, X. Liu and M. Ye, *ACS Appl. Mater. Interfaces*, 2020, **12**, 6442–6450.

166 R. Saraf, L. Pu and V. Maheshwari, *Adv. Mater.*, 2018, **30**, 1705778.

167 V. Jella, S. Ippili, J.-H. Eom, J. Choi and S.-G. Yoon, *Nano Energy*, 2018, **53**, 46–56.

168 A. Sultana, M. M. Alam, K. Roy, P. Sadhukhan, S. Das, S. Sarkar, T. R. Middya and D. Mandal, *Mater. Res. Express*, 2019, **6**, 115709.

169 J.-H. Eom, H.-J. Choi, S. V. N. Pammi, V.-D. Tran, Y.-J. Kim, H.-J. Kim and S.-G. Yoon, *J. Mater. Chem. C*, 2018, **6**, 2786–2792.

170 R. Saraf, T. Tsui and V. Maheshwari, *J. Mater. Chem. A*, 2019, **7**, 14192–14198.



171 J. W. Fergus, *Sens. Actuators, B*, 2007, **123**, 1169–1179.

172 Y. Shimizu and N. Yamashita, *Sens. Actuators, B*, 2000, **64**, 102–106.

173 A. Maity, A. K. Raychaudhuri and B. Ghosh, *Sci. Rep.*, 2019, **9**, 7777.

174 Y. Wang, J. Chen and X. Wu, *Mater. Lett.*, 2001, **49**, 361–364.

175 K. Abisegapriyan, N. P. M. J. Raj, N. R. Alluri, A. Chandrasekhar and S.-J. Kim, *Sens. Actuators, B*, 2020, **320**, 128417.

176 Y. Zhao and K. Zhu, *Chem. Commun.*, 2014, **50**, 1605–1607.

177 R. Kour, S. Arya, S. Verma, J. Gupta, P. Bandhoria, V. Bharti, R. Datt and V. Gupta, *Global Challenges*, 2019, **3**, 1900050.

178 C. Liu, W. Li, J. Fan and Y. Mai, *J. Energy Chem.*, 2018, **27**, 1054–1066.

179 B. Wang, J. Iocozzia, M. Zhang, M. Ye, S. Yan, H. Jin, S. Wang, Z. Zou and Z. Lin, *Chem. Soc. Rev.*, 2019, **48**, 4854–4891.

180 S. Wang, L. Li, W. Weng, C. Ji, X. Liu, Z. Sun, W. Lin, M. Hong and J. Luo, *J. Am. Chem. Soc.*, 2019, **142**, 55–59.

181 X. Liu, S. Wang, P. Long, L. Li, Y. Peng, Z. Xu, S. Han, Z. Sun, M. Hong and J. Luo, *Angew. Chem., Int. Ed.*, 2019, **58**, 14504–14508.

182 Y. J. Yoon, Y. Chang, S. Zhang, M. Zhang, S. Pan, Y. He, C. H. Lin, S. Yu, Y. Chen and Z. Wang, *Adv. Mater.*, 2019, **31**, 1901602.

